2003-08

A Neural Model of Surface Perception: Lightness, Anchoring, and Filling-in

A neural model of surface perception: Lightness, anchoring, and filling-in

Stephen Grossberg and Simon Hong

August, 2003

Technical Report CAS/CNS-2003-016

Boston University Center for Adaptive Systems and

Department of Cognitive and Neural Systems

677 Beacon Street

Boston, MA 02215

A Neural Model of Surface Perception: Lightness, Anchoring, and Filling-In

Stephen Grossberg and Simon Hong*

Department of Cognitive and Neural Systems
And
Center for Adaptive Systems
Boston University
677 Beacon Street, Boston, MA 02215, USA

Abbreviated title: A Neural Model of Surface Lightness Perception

August 2003

Technical Report CAS/CNS TR-2003-016

All correspondence should be addressed to
Professor Stephen Grossberg
Department of Cognitive and Neural Systems
Boston University
677 Beacon Street
Boston, MA 02215
Phone: 617-353-7858
Fax: 617-353-7755
Email: steve@bu.edu

* Authorship in alphabetical order. SG and SH were supported in part by the Air Force Office of Scientific Research (AFOSR F49620-01-1-0397), the Defense Advanced Research Projects Agency and the Office of Naval Research (ONR N00014-95-1-0409), and the Office of Naval Research (ONR N00014-01-1-0624).

Abstract

This article develops a neural model of how the visual system processes natural images under variable illumination conditions to generate surface lightness percepts. Previous models have clarified how the brain can compute the relative contrast of images from variably illuminated scenes. How the brain determines an absolute lightness scale that "anchors" percepts of surface lightness to use the full dynamic range of neurons remains an unsolved problem. Lightness anchoring properties include articulation, insulation, configuration, and area effects. The model quantitatively simulates these and other lightness data such as discounting the illuminant, the double brilliant illusion, lightness constancy and contrast, Mondrian contrast constancy, and the Craik-O'Brien-Cornsweet illusion. The model also clarifies the functional significance for lightness perception of anatomical and neurophysiological data, including gain control at retinal photoreceptors, and spatial contrast adaptation at the negative feedback circuit between the inner segment of photoreceptors and interacting horizontal cells. The model retina can hereby adjust its sensitivity to input intensities ranging from dim moonlight to dazzling sunlight. At later model cortical processing stages, boundary representations gate the filling-in of surface lightness via long-range horizontal connections. Variants of this filling-in mechanism run 100-1000 times faster than diffusion mechanisms of previous biological filling-in models, and shows how filling-in can occur at realistic speeds. A new anchoring mechanism called the Blurred-Highest-Luminance-As-White (BHLAW) rule helps simulate how surface lightness becomes sensitive to the spatial scale of objects in a scene. The model is also able to process natural images under variable lighting conditions.

Keywords: Surface perception, Lightness, Anchoring, Filling-in, Retinal adaptation

1. Introduction

The human visual system perceives surface reflectance (percent of light reflected by a surface in each wavelength) with remarkable fidelity even under greatly varying illumination conditions. The retina receives luminance signals, which are a product of reflectances and illumination levels (Hurlbert, 1989), from objects in the world, rather than the reflectances that are a property of object surfaces. From these luminance signals, the visual system needs to discount the illuminant to discover the reflectances themselves by using contextual cues, including cues of illumination (Figure 1). Discounting the illuminant is not sufficient, however, because the illuminant-discounted signals characterize only the relative amounts of light that each object surface reflects to the eyes. For effective perception, the brain also needs to discover an *absolute* lightness that can represent the full-range of experience from dim moonlight to dazzling sunlight. The present article describes a neural model that contributes to understanding how such an absolute lightness is constructed by the brain from the illuminant-contaminated signals that are received at our retinas.

Retinal preprocessing of visual signals contributes greatly to discovering an absolute lightness scale. These processes include two mechanisms of gain control: Light adaptation and contrast adaptation. Human vision adapts to ten orders of magnitude of daily variations of ambient illumination (Martin, 1983). For example, if the brain gets an input like the one in Figure 2A, it would "see" it like the one in Figure 2B. This property, termed *light adaptation*, depends in part on retinal circuitry (Werblin, 1971). Figure 2C shows the model response to varying background illumination. The graph illustrates how the range of maximal sensitivity of an early stage of model adaptation shifts with background illumination without undergoing compression, as also occurs in the retina (Werblin, 1971). Another dimension of adaptation is spatial *contrast adaptation*. For example, if there is a big contrast in the visual field such as the one in Figure 2D, the brain can, under a wide range of viewing conditions, properly rescale input signals to see the dark side as well as the bright side of the scene, as in the model simulation of Figure 2E. Since retinal ganglion cells, which are the sole output units of the retina, have firing rates that vary over less than three orders of magnitude, the visual system needs to compress the

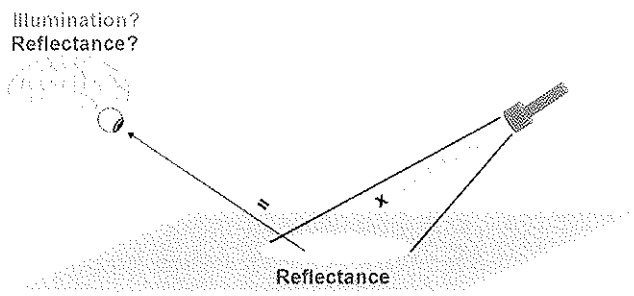

Figure 1. What the visual system sees is luminance, a product of reflectance and illumination. The visual system attempts to estimate the reflectance using available illumination cues.

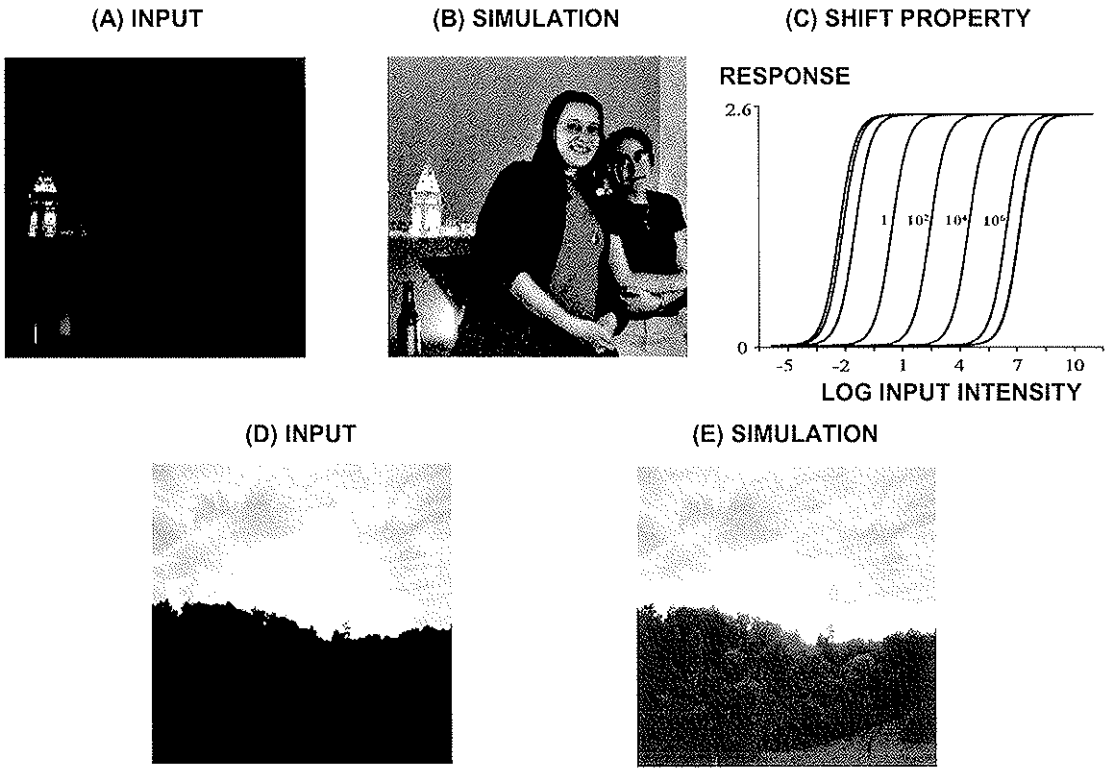

Figure 2. Retinal adaptation. (A-B) Input and the simulation of the model reflecting the result of light adaptation of the retina. (C) Shift property of sensitivity of the model retinal units. The model retina simulates the light adaptation property by automatically shifting its operating range to adapt to the ambient luminance of the visual field. When the luminance is too low, it simulates the physical limit of adaptation (the saturation of shifting on the left end of the graph). For clarity only four mean input intensities are shown besides the corresponding curves. The visible 3 leftmost curves have mean luminances of 10^{-4}, 10^{-3}, and 10^{-2} from the left-end, respectively. The visible rightmost curve has a mean luminance of 10^{7}. (D-E) Input with high spatial contrast and the model simulation of the input. It is assumed that the retinal circuit is responsible for this kind of non-linear rescaling of contrast that makes the brain "see" the dark part as well as the bright part. Photo courtesy of Arash Fazl and Bob Wagner.

dynamic range of input at the retinal level, without a loss of sensitivity. Currently, the mechanisms of spatial as well as temporal component of contrast adaptation are still undergoing intensive experimental investigation (Demb, 2002; Baccus & Meister, 2002). Some of the gain-control mechanisms of the retina contributing to these adaptations may include: (1) Ca^{2+} ion-mediated negative feedback occurring at the photoreceptors (Koutalos & Yau, 1996) and bipolar cells (Nawy, 2000); (2) bleaching of photopigments (Dowling, 1987; Fain, 2001); (3) surround negative feedback by the horizontal cell (HC) network (McMahon et al., 2001; Thibos & Werblin 1978; Werblin, 1974); and (4) a circuitry switch from cones to rods (Mills & Massey, 1995; Ribelayga, Wang & Mangel, 2002). Such mechanisms enable cells to dynamically change their operating range to adapt to varying lighting situations.

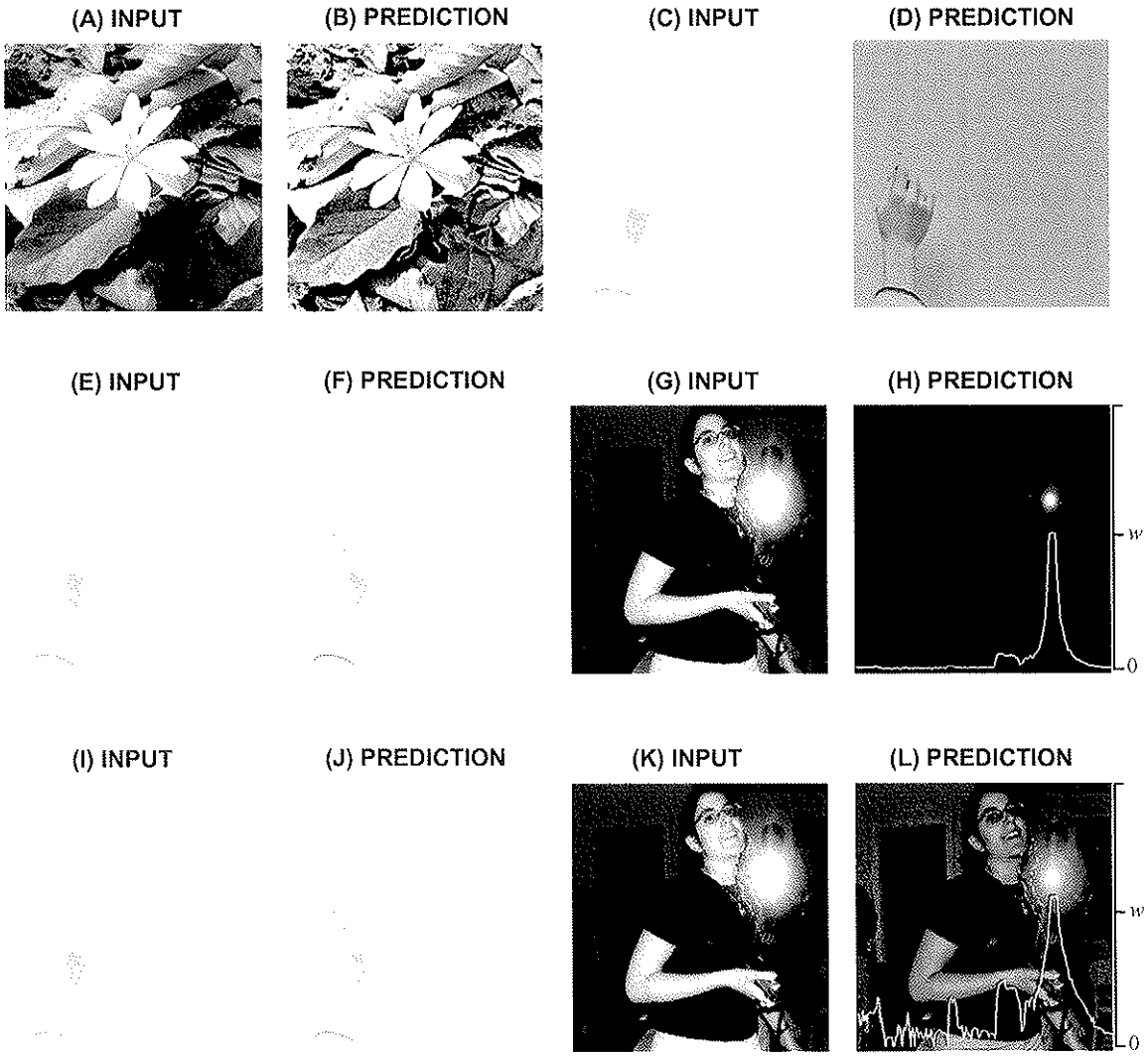

Figure 3. Predictions by various lightness theories. (A-B) Input and correct prediction of lightness by *average luminance rule*. (C-D) Input and wrong prediction by *average luminance rule*. According to *average luminance rule*, the whiteboard should look middle gray. (E-F) Input and correct prediction of lightness by *Highest-luminance-as-white* (HLAW) rule. (G-H) Example where HLAW rule makes an error. HLAW rule makes an error due to a prominent highest luminance like the one in (G). (I-L) Inputs and corresponding predictions made by the model developed here. The model with a new rule called *blurred-highest-luminance-as-white* (BHLAW) rule correctly predicts percepts. See the text for further explanations.

Surface lightness percepts cannot, however, fully be explained by such low-level mechanisms. For example, visual percepts depend upon appropriate interactions between both ON and OFF channel signals that seem to be largely segregated up until cortical area V1 (Schiller, Sandell & Maunsell, 1986; Schiller, 1992). Attempts to explain surface lightness range from the classic *inference* theory of Helmholtz (1866) to recent theories that Gilchrist and his colleagues classify as *intrinsic image* theories (Arend 1994; Gilchrist et. al., 1999). While several theories propose that lightness is derived from luminance ratios among surfaces in a display,

these computations can, at best, recover relative reflectances. Thus there still remains the problem of systematically mapping these relatively defined lightness values to the absolute lightness values that are experienced during visible percepts. One proposed possible solution is the *average luminance rule* suggested by Helson (1943). This hypothesis proposes that the average luminance of the display, defined as middle gray, acts as a standard "anchoring" point for other luminances. For example, higher luminances than the average luminance will be assigned higher values of lightness than middle gray. Figures 3A and 3B show an example where this rule makes a correct prediction. However, when the rule meets a situation like the one in Figure 3C, it make the error shown in Figure 3D: The whiteboard becomes middle gray. As the example shows, the *average luminance rule* does not explain lightness data quantitatively.

In one of the first attempts to quantify lightness, Wallach introduced an anchoring hypothesis which became known as *highest-luminance-as-white* (HLAW) rule (Horn 1977; Land & McCann, 1971; Wallach, 1948, 1976). This rule assumes that the perceptual quantity "white" is assigned to the highest luminance in a given scene as the standard, and that lower luminant surfaces are assigned to gray values relative to it. According to this rule, the whiteboard in Figure 3E should look white, as in Figure 3F. In cases where there is a highest luminance like the one in Figure 3G, however, the HLAW rule makes a wrong prediction, as shown in Figure 3H. The white curve in Figure 3H that is superimposed on the image shows the profile of the predicted lightness along the horizontal section of the image that crosses the light source. The value "*w*" on the right side of Figure 3H marks the lightness value "white" along the vertical axis. By converting the intense illumination source into "white," the HLAW rule drives all other lightness values to unacceptably small levels.

To overcome these shortcomings of previous hypotheses, the current model, which was briefly reported in Hong and Grossberg (2003), proposes how brain dynamics may instantiate a new rule called the *blurred-highest-luminance-as-white* (BHLAW) rule. The blurring part, which is spatial integration, makes the model sensitive to the area subtended by the highest luminance, thus introducing spatial-scale into the assessment of surface lightness (Figure 4A). This mechanism also enables this model to explain the self-luminosity of certain surface regions (Figure 4B). See Section 2.5 for further explanation.

Figures 3I, 3J show model's property that is similar to HLAW rule. Figures 3K and 3L show the distinct property of the model that correctly predicts the lightness of the surface, despite the light source in the input. The curve on Figure 3L shows the profile of the simulated lightness of the horizontal section of the image that crosses the light source. The peak of the curve going above white "*w*" predicts that the light source will look self-luminous. By incorporating a BHLAW process into a multi-stage model of boundary and surface processing, the model also explains, among other lightness data, the four sets of data that Gilchrist and his colleagues (1999)

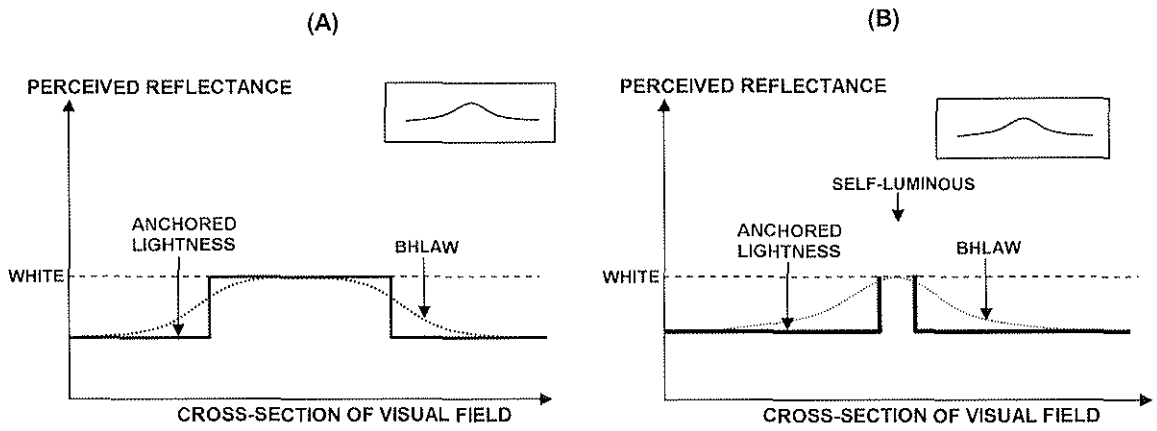

Figure 4. *Blurred-highest-luminance-as-white* (BHLAW) rule and spatial scale. (A) BHLAW rule with a large area of highest luminance. The dashed line indicates the value of WHITE which the blurred highest luminance attains. The thick line (ANCHORED LIGHTNESS) illustrates a 1-D profile of the anchored lightness. In this example, the blurred highest luminance equals white because the area of the highest luminance is at least as large as the kernel used for blurring in the BHLAW module (the inset). (B) BHLAW rule with a small area of highest luminance. Here the blurred highest luminance is smaller than the highest luminance because of the small size of the area of highest luminance relative to the blurring kernel. When the blurred highest luminance is anchored at white, the highest luminance gets pushed above white, becoming self-luminous.

have proposed should be explained by any quantitative lightness theory. These four factors in lightness assignment are Articulation, Configuration, Insulation, and the Area Effect.

Figures 5A to 5E illustrate the procedure and the percepts of the Articulation Effect: A black patch (reflectance 3%) is fixed in front of a homogenous dark background (Figure 5A). When the patch gets illumination 30 times that of the dark background resulting in the luminance of 1.4 ftL (foot Lambert), it looks white (Figure 5B). (This 30-to-1 foreground-background illumination setting is also used in the following Configuration, Insulation, and the Area effects). When a real white patch (reflectance 90%) appears near the white-looking black patch, the black patch appears gray (Figure 5C). In the experiment, the subjects indicated the perceived reflectance by selecting a match from a Munsell chart of 16 examples near the subject. The Munsell chart was illuminated with a different light source so that the luminance of the whitest white, Munsell 9.5, was 160 ftL. The phenomenon illustrated in Figures 5B and 5C is called Gelb effect (for further discussion, see Cataliotti & Gilchrist, 1995). As more gray patches are added, the dark ones look darker and darker (Figures 5D and 5E). This darkening effect does not affect the highest luminance surface, which remains "anchored" to white. The graph in Figure 5F shows data that summarize this effect. Figure 5G shows the model simulation of these data. It should be noted that even in the two-Mondrian case in Figure 5C, the reflectances of these patches range from black to white covering the full span of reflectance used in the experiment. Thus the process of adding different luminance patches is just a process of "articulation". This effect may not necessarily need patches of many different levels of luminance. For example, one

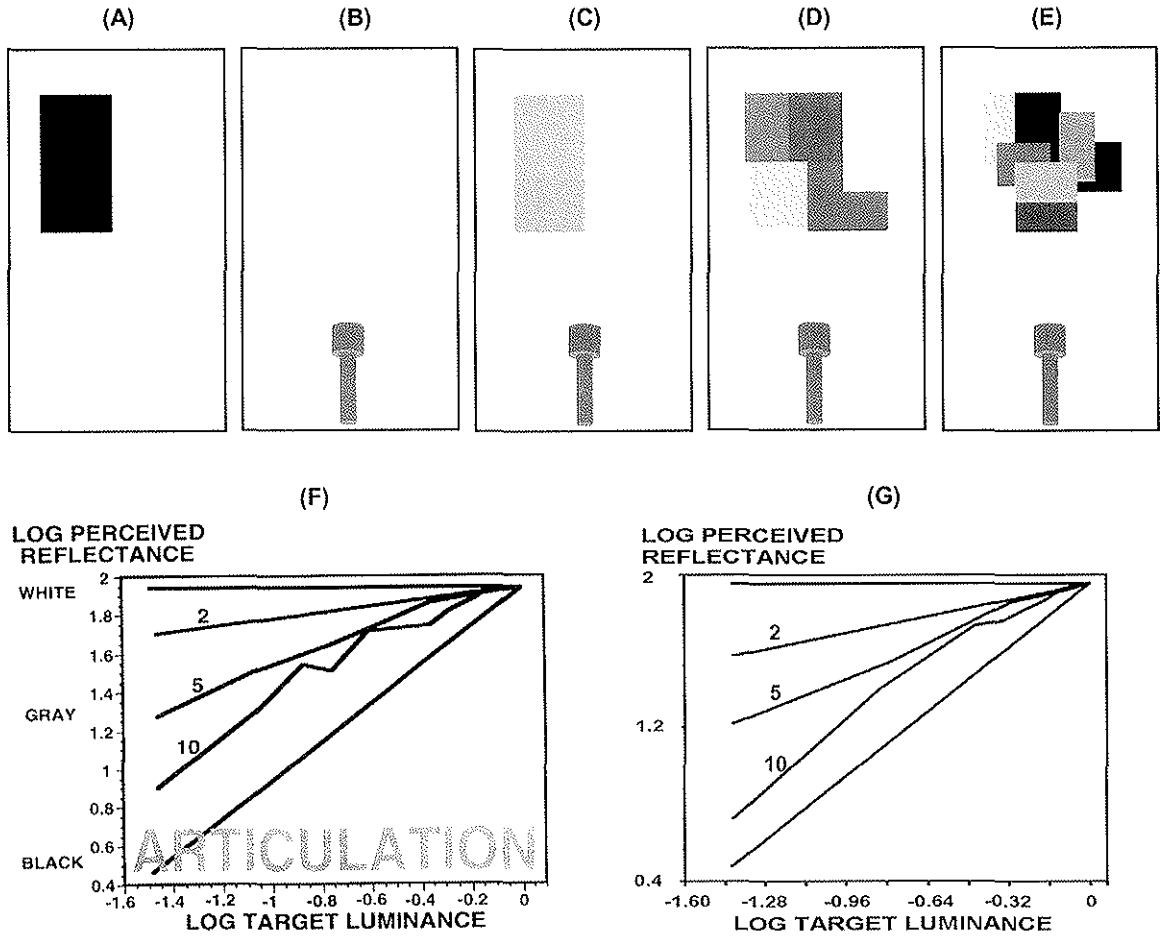

Figure 5. Articulation effect. (A-E) Illustration of the procedure and percepts of Articulation effect experiment. See the text for details. The patterned backgrounds illustrate the dark background in the experiment. (F) Data of Articulation effect. As more gray patches are added to a display, the range of perceived reflectance (lightness) widens. In the graph, the widening of the perceived reflectance corresponds to the steeper overall curve as the number of gray level target surfaces increases from one to ten as illustrated in B to E. The widening effect makes the gray patches look darker. The diagonal line shows the perfect situation of lightness constancy. The horizontal line shows the situation where there is just one surface on the Ganzfeld (a homogeneous background covering the entire visual field with no other visual cues). (G) Simulation results. PERCEIVED REFLECTANCE in the model is ANCHORED LIGHTNESS of the simulation. See the text for details. Figure F is from Gilchrist et al. (1999).

large white surface and one gray surface will give a smaller perceived lightness difference than in the situation where the two large surfaces are divided into small pieces and intermingled. See the text below for further explanation.

Figures 6A and 6B illustrate the procedure and the percepts of the Configuration Effect: A Mondrian display in Figure 6B—namely, a 2-D arrangement of juxtaposed gray patches—widens the range of perceived reflectance compared to the linear arrangement of patches shown in Figure 6A. Said more simply, the dark patches in Figure 6A appear lighter than the corresponding dark patches in Figure 6B. Graphs in Figures 6C and 6D show data that summarize this effect. Comparison of the graphs 6C and 6D shows that this effect becomes

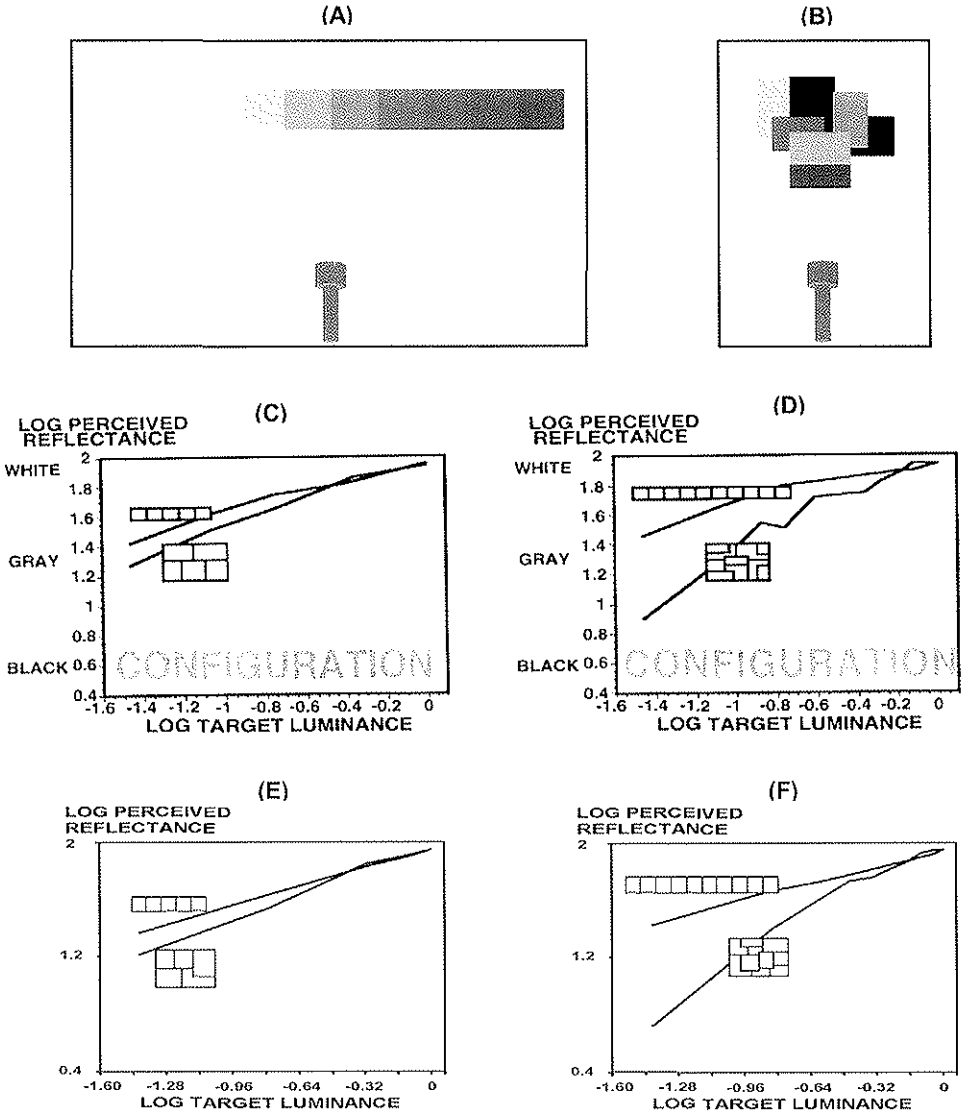

Figure 6. Configuration effect. (A-B) Illustration of the experimental settings and the percepts of Configuration effect. See the text for details. (C-D) Data of Configuration effect. The lower inset of each figure shows the Mondrian arrangement; the upper inset, staircase arrangement. Mondrian arrangement of gray target surfaces widens the range of lightness compared to the staircase arrangement. Comparison of C and D shows that articulation makes the effect bigger. (E-F) Simulation results, corresponding C and D, respectively. The model fits the data of configuration effect in the anchoring theory. See the text for details. The figures C, D are from Gilchrist et al. (1999).

greater with more local articulation. Figures 6E and 6F show model simulation results. See the text below for further details.

Figures 7A to 7C show the procedure and the percepts of the Insulation Effect: When the staircase arrangement is surrounded by a white insulating region, the range of perceived reflectance widens (Figure 7B). The widening of the range of perceived lightness in a frame does not occur when the staircase is insulated by a black border (Figure 7C). The graph in Figure 7D

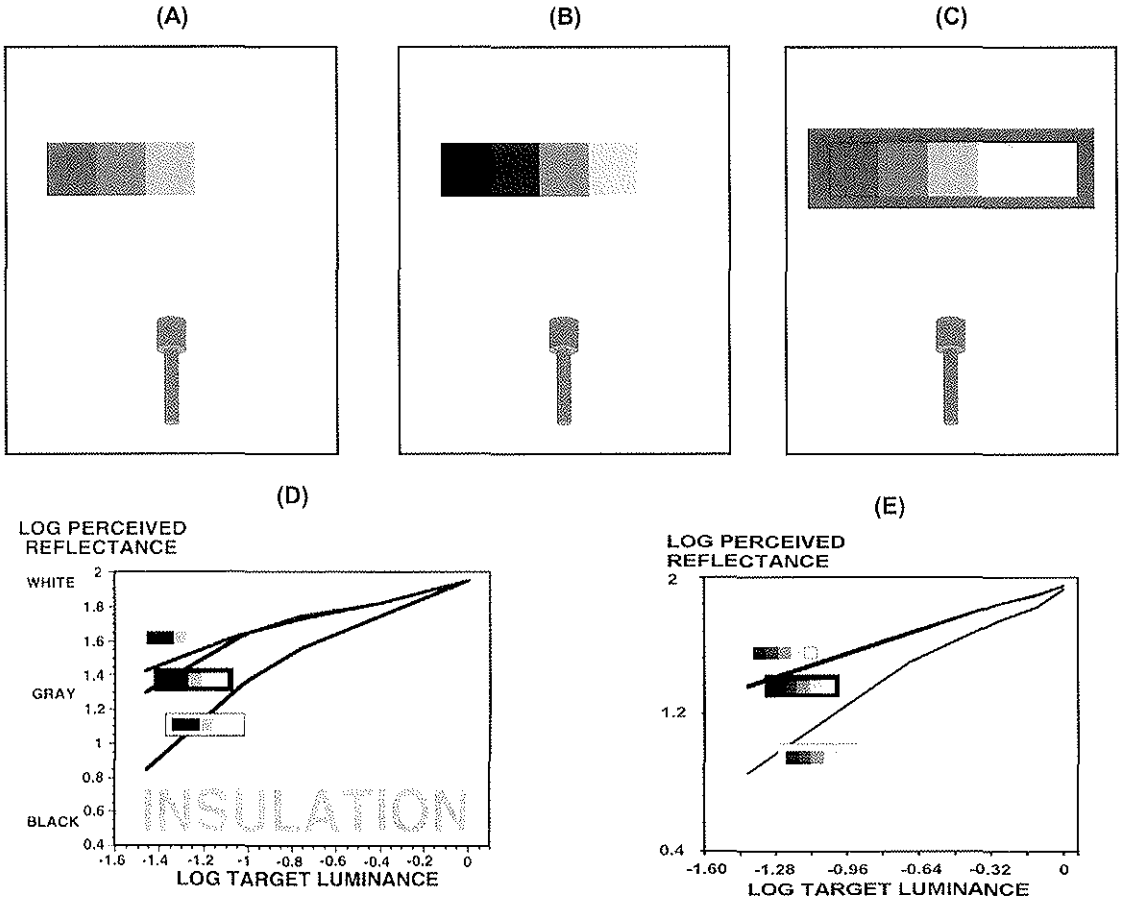

Figure 7. Insulation effect. (A-C) Illustration of the experimental settings and the percepts of Insulation effect. See the text for details. (D) Data of Insulation effect. Insulation by a white surrounding widens the range of perceived reflectance. This effect does not seem to happen when a black surrounding is used for insulation. (E) Simulation results. The model fits the data of configuration effect in the anchoring theory. See the text for further explanation. Figure D is from Gilchrist et al. (1999).

summarizes data showing this effect. Figure 7E shows the model simulation of these data. See the text below for further explanation.

The lower part of Figure 8A shows the experiment setting for the Area Effect. The head of the subject is covered by a dome that is divided into two regions. The upper part of Figure 8A illustrates the stimuli and the corresponding percepts. When the highest luminance area occupies more than half of the visual field, it appears white while the darker part looks gray. As the darker area occupies more than half of the visual field, however, it approaches white, while the lighter area gets pushed above white and appears self-luminous. The data curves in Figure 8B show this effect. Figure 8C shows the simulation results. See the text below for further explanation.

No published models have yet explained how these various data can be explained using an anchoring process, among other stages in the processing of lightness information. This study develops a biologically plausible model that explains and simulates a wide range of lightness data, including these data of Gilchrist and his colleagues.

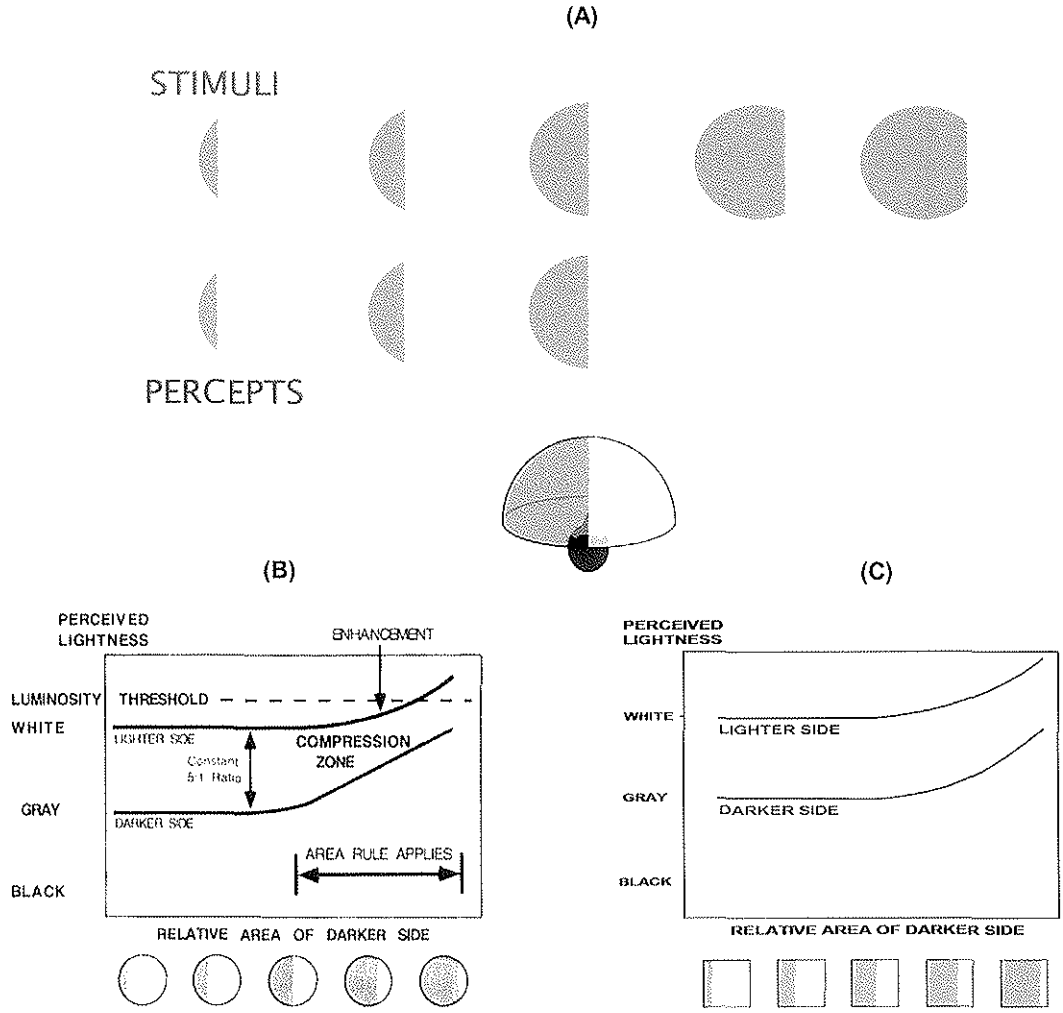

Figure 8. Area effect in divided Ganzfeld situation. (A) Illustration of the experimental settings and the percepts of Area effect. See the text for details. (B) Qualitative illustration of the area effect. As the non-highest luminance area becomes bigger than the half of the visual field, it approach to white, while the smaller area of highest luminance becomes luminous. The divided discs along the abscissa with light and dark surfaces show the configurations of the stimuli. (C) Simulation result of Area effect. The model simulates the concept of the effect quantitatively. The squares along the abscissa with light and dark surfaces show the configurations of the stimuli. See the text for details. Figure B is from Gilchrist et al. (1999).

2. Description of The Model

Figure 9 illustrates the model. The first stage adapts to ambient luminance and spatial contrasts. Using the adapted signal, the next stage generates contrast signals using multiple-scales of antagonistic ON-center OFF-surround and OFF-center ON-surround processes (see the following descriptions). The light-adapted signal itself also goes via a parallel pathway to the next level without change as the luminance signal. The process then branches into two streams: The boundary and surface processing streams, which have previously been modeled as the Boundary

Contour System (BCS) and Feature Contour System (FCS), respectively (Grossberg, 1994, 1997; Grossberg and Kelly, 1999; Grossberg and Mingolla, 1985a, 1985b; Grossberg and Todorovic, 1988; Kelly and Grossberg, 2000). The luminance and contrast signals are pooled at the filling-in stage of the surface system, where their spread is gated, or blocked, by boundary signals. At the final stage, the filled-in signals are rescaled via an anchoring process to assign appropriate lightness values. The anchored signals represent the perceived lightness in the model.

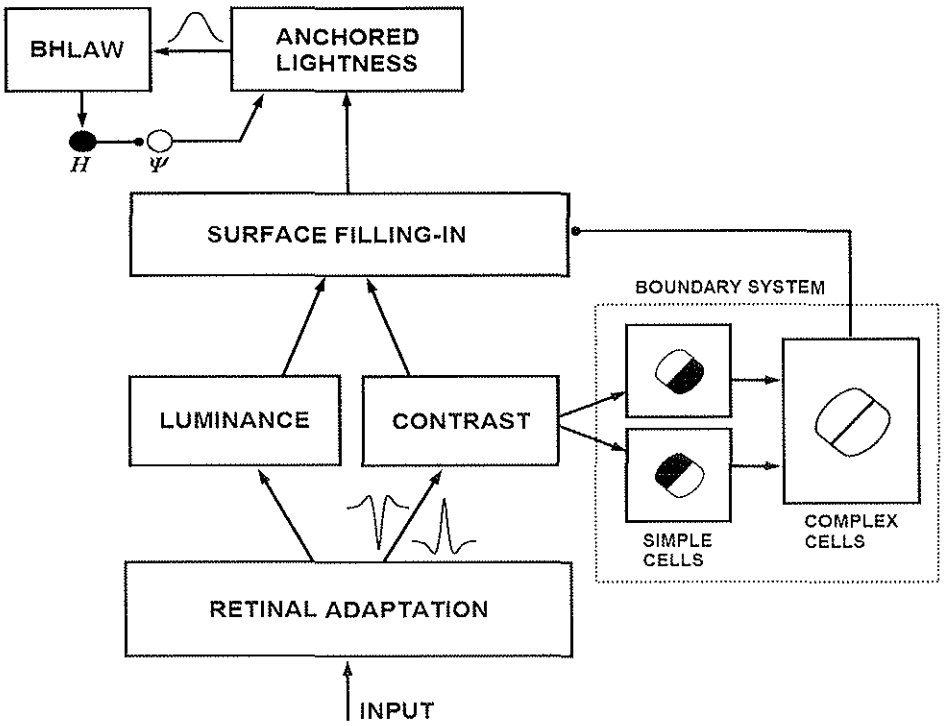

Figure 9. Illustration of the model. See the text for details. Each box indicates an array of cells doing a similar task. Arrow-heads indicate excitatory signals for the post-synaptic units; round-heads indicate inhibitory. The Mexican-hat shape and the up-side-down shape of it between the RETINAL ADAPTATION and CONTRAST modules illustrate the one-dimensional shapes of the on-center off-surround and off-center on-surround antagonistic filters for contrast calculation. The bell-shaped curve between the ANCHORED LIGHTNESS and BHLAW (Blurred-Highest-Luminance-As-White) modules illustrates the one-dimensional shape of the blurring kernel for anchoring. For clarity, BOUNDARY SYSTEM shows just one orientation. In the simulation, four orientations are used.

2.1 Retinal Adaptation

This stage of the model calculates the steady-state of retinal adaptation (light adaptation and spatial contrast adaptation) to a given input image. Using an intracellular gating mechanism at the outer-segment of the photoreceptor, the model first shifts the sensitivity curve of the photoreceptor and computes a light-adapted signal (GATED INPUT in Figure 10) at each position of the visual field (Baylor, Hodgkin & Lamb, 1974a, 1974b; Carpenter & Grossberg, 1981; Koutalos & Yau, 1996). This light-adapted signal is further processed at the inner segment

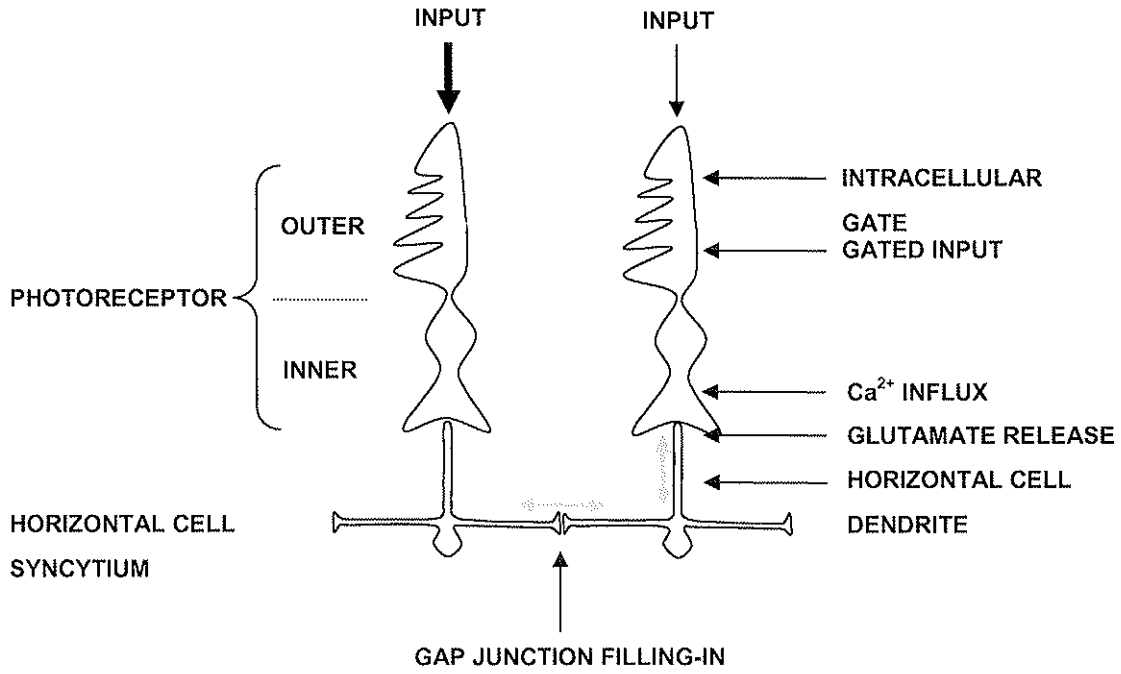

Figure 10. Circuit of retinal adaptation. Two stages of Retinal adaptation are implemented: One light adaptation at the outer segment of the photoreceptors, the other, spatial contrast adaptation at the negative feedback circuit between the inner-segments of photoreceptors and a syncytium of HCs. It is assumed that the permeability of the gap junctions between HCs decreases as the difference of the inputs to the HCs from the coupled photoreceptors increases. For simplicity only the connections between nearest neighbors are shown. In simulations, long-range connections are also allowed. The gray bidirectional arrows show the mutual influence between connected units. See the text and Appendix for further details.

of the photoreceptor where it gets feedback from the horizontal cell (HC) that is connected with other HCs by gap junctions, forming a syncytium (Figure 10). This HC inhibition is hypothesized to further adjust the sensitivity curve of the photoreceptor for spatial contrast adaptation.

It is assumed that the permeability of the gap junctions between HCs decreases as the difference of the inputs to the HCs from the coupled photoreceptors increases. In the situation shown in Figure 10, for example, where the input for the network has a steep difference (the thick and thin input arrows), the permeability between the left and right HCs will decrease. When there is not much difference in inputs for connected photoreceptors, the permeability between the HCs will remain large. Through this mechanism, the model retina can rapidly segregate and selectively suppress the signals in areas that have strong contrasts, such as a light source. For clarity, Figure 10 shows only the connections between nearest neighbors. In simulations, connections reaching farther than nearest neighbors are also used that model the connectivity and cell types in the retina (Masland, 2001; Sterling, 1998). It is hypothesized that the inhibition of the HC on the photoreceptor controls the output of the photoreceptor

(GLUTAMATE RELEASE in Figure 10) by modulating the Ca^{2+} influx at the inner segment of the photoreceptor. This feedback prevents the output from saturation by localized high-contrast input signals. Thus this mechanism helps us see the room lit by a light bulb, the light bulb itself, and the label on it. See Appendix A for mathematical details.

2.2 Multiple-Scale Contrast and Luminance Stage

The retinally-adapted signal is processed by the center-surround contrast stage. The separation of the initial stage of retinal adaptation from the following center-surround stages seems to benefit the visual system in several ways: (1) The subsequent stages do not have to handle the light itself as the input anymore. They are cushioned from the impact of the vastly varying external inputs and receive normalized input signals. (2) The contrast stage is assumed to concentrate on spatial frequency-specific processing in multiple scales, extracting salient information for each spatial frequency. In the model, this stage simulates the cell types having concentric receptive fields of on-center off-surround or off-center on-surround found in the retina (Barlow, 1953; Cook and McReynolds, 1998; Kuffler, 1953; Werblin & Dowling, 1969) and the lateral geniculate nucleus (LGN) (Dubin & Cleland 1977; Hubel & Wiesel, 1961; Jones et. al., 2000). The model on-center off-surround (ON) units are excited by signals falling on the central part of their receptive fields, while they become suppressed when light falls on the surround of their receptive fields. This is implemented by a combination of a narrow excitatory Gaussian filter for the center and a broad inhibitory Gaussian filter for the surround. The model off-center on-surround (OFF) units increase their activities when a light stimulus falls on their surround receptive field and decrease their activities when a stimulus falls on the center part of the receptive field (Schiller 1992).

The 1-D cross-sections of the contrast operators are illustrated in Figure 9 between the RETINAL ADAPTATION and CONTRAST stages. Using feed-forward shunting equations (Grossberg 1983; see the equation below), the operation extracts local contrasts. In the case of an on-center off-surround network, for example, this process effectively eliminates the illumination influence on the local input in a scale-specific manner by dividing the input of the center by the local average represented by the surround, thus estimating the local contrast:

$$\text{Contrast} = \frac{L_{spot} - L_{background}}{L_{spot} + L_{background}},$$

where L_{spot}, and $L_{background}$ are the luminances of the probe stimulus and background, respectively. Using different sizes of surround, the system extracts small-scale to large-scale contrasts. These various surround sizes simulate the different sizes of lateral inhibition cell types in the retina (for a review, see Masland, 2001). The model uses a fixed narrow center kernel with the different surround scales (Grossberg et al, 1995; Mingolla et al, 1999) and thereby also simulates the output of a sharp center at the ganglion cells due to interactions in the retinal

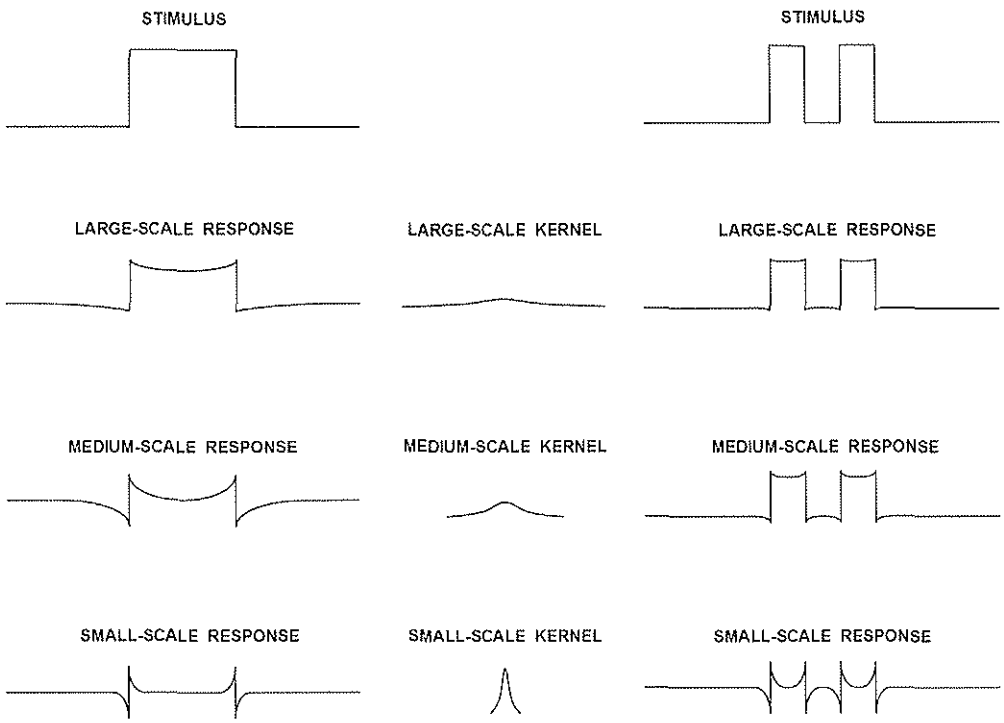

Figure 11. One-dimensional illustration of center-surround processes in different spatial scales. The figure shows two stimuli and corresponding processed signals in different spatial scales in the left, right columns. The surround kernels of different spatial-scales are shown in the middle column. For clarity, the narrow center kernels, whose sizes are the same, are not shown. As a given surface divides into smaller patches, such as from the stimulus on the left to the stimulus on the right, medium and large-scale center-surround processes do not fully activate and fully suppress the homogeneous area. Since the model uses the weighted sum of multiple scale signals, this leads to a more veridical or non-compressed representation. The model takes this contrast calculation mechanism as part of the Articulation, Configuration, and Insulation effects of lightness anchoring. See Lightness Anchoring section for further details.

network (Cook and McReynolds, 1998; Roska et al., 2000). All discussion of multiple spatial scales in this study is restricted to scales of surround kernels. This simplification reflects our minimal approach to designing a model capable of explaining various lightness data. Although the center-surround process is presented separately from the retinal adaptation stage, it also contributes to background adaptation. In the same vein, the adaptation carried by the photoreceptor and HCs is a type of center-surround process with a large surround scale.

Multiple scales, which are defined by the width of the Gaussian filters, contribute with different weights to form a complete representation of the stimulus. Figure 11 illustrates how three different scales respond to luminance inputs. Since the large-scale signal tends to represent the luminance signal more veridically (see LARGE-SCALE RESPONSE in Figure 11), we call this as *luminance signal*. A scale that is small relative to a given image region may exhibit a property known as *brightness bowing* (see SMALL-SCALE RESPONSE in Figure 11). In order to preserve the resolution of the image, single-scale models typically use such small scales, while

omitting bigger scales. The brightness bowing property stems from the fact that a small-scale (high frequency) center-surround unit acts like an edge detector of luminance boundaries, and thereby suppresses information from large homogeneous surface parts. Summation of multiple scales naturally compensates for this problem.

This multiple-scale property of the model is consistent with electrophysiological observations in V1 of alert primates (Bartlett & Doty, 1974; Kayama et al., 1979; Kinoshita & Komatsu, 2001; Komatsu, Murakami & Kinoshita, 1996) and anesthetized cats (MacEvoy, Kim & Paradiso, 1998), where cells not only code edge signals but also uniform surface luminance as well. A recent electrophysiology study with alert monkeys by Friedman et al. (2003) also shows that cells in V1 and V2 code uniform color surface information. For the LGN, uniform surface luminance coding units have been found in anesthetized primates (Marrocco, 1972) and cats (Papaioannou & White, 1972) as well as in alert primates (Barlow, Snodderly & Swadlow, 1978; Kayama et al., 1979). When surface luminance was temporally modulated, the cells in the LGN and V1 of anesthetized cats coding the surface region were modulated (Rossi et al, 1996; Rossi & Paradiso, 1999). Bartlett and his colleagues (1980) failed to detect such neurons in visual cortex of the awake rabbit. Their data suggest that there may be some differences between species, and techniques of anesthesia also seem to play an important role.

2.3 Boundary Formation

In surface perception, the boundaries defining a surface are prominent cues. Boundary formation as a factor in surface percept generation has been recognized by the Gestalt psychologists (Koffka, 1935), and used to model psychophysical and neural data about surface perception (Arrington, 1994; Cohen & Grossberg, 1984; Grossberg & Mingolla, 1985a, 1985b; Grossberg & Kelly, 1999; Grossberg, Hwang & Mingolla, 2002; Kelly & Grossberg, 2000; Pessoa, Mingolla & Neumann, 1995). Grossberg & Todorović (1988) developed this concept to simulate psychophysical data about brightness (perceived luminance). In their model, a center-surround network among cells obeying membrane equations discounts the illuminant. The surviving contrast signals are used to fill-in a surface brightness estimate within a region surrounded by boundaries that are themselves derived from the illuminant-discounted contrast signals (see the following Filling-In section for more details). The current model adopts this hypothesis to explain lightness data using contrast and luminance signals together to fill-in a region defined by surrounding boundaries (Figure 9).

Boundary formation begins at model simple cells that simulate orientationally-tuned simple cells in layer 4 of cortical area V1 (Figure 9), which have contrast-polarized and oriented ON (excitatory for luminance) and OFF (excitatory for darkness) regions in their receptive fields (Bullier and Henry 1979; Gilbert 1977; Hubel and Wiesel 1962). The model simple cells pool

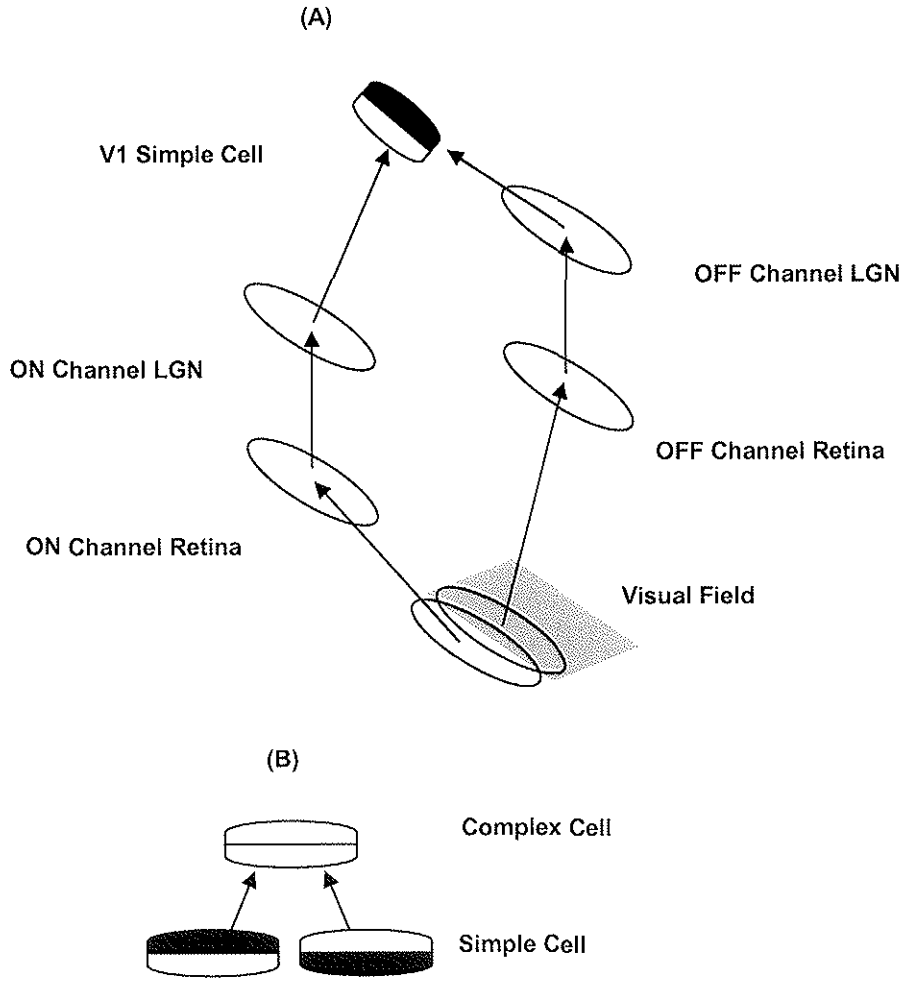

Figure 12. The assumed circuits for the simple cell and complex cell. (A) Simple cell circuitry. The simple cell (the half-filled half-hollow symbol at the top) pools the signals from the ON cells and the OFF cells of the LGN. The arrows show the flow of signals. The elongated ellipses at the Visual Field represent the simple cell's sub-receptive fields. The other ellipses represent the involved cell groups in the signal flow. Each parallelogram for the retina, LGN and V1 represents an array of regularly dispersed cell groups. In the figure, the luminance contrast stimulus at the Visual Field can activate the model simple cell. See the text for details. Adapted from Lee et al. (2000). (B) Complex cell circuitry. A pair of light-dark and dark-light simple cell signals of the same orientation at each position is pooled for the complex cell of the same orientation.

model ON cell LGN outputs in their ON region and OFF cell LGN outputs in their OFF region. This is consistent with the observation that the ON and OFF subfield properties of simple cells seem to originate from the projections of ON and OFF cells in the LGN, respectively (Alonso, Usrey & Reid 2001; Lee et al., 2000; Reid & Alonso, 1995). Figure 12A shows the assumed input circuit for the model simple cell. These receptive field properties of a simple cell are modeled by a pair of elongated Gaussian kernels with shifted centers (Grossberg, Mingolla & Williamson, 1995; Mingolla, Ross & Grossberg, 1999; Pessoa, Mingolla & Neumann, 1995). Since the ON and OFF regions are spatially oriented and juxtaposed, the model simple cell is

maximally active when there is a luminance edge aligned with the oriented border between the ON and OFF regions. This property comes from the design of the ON and OFF regions made of Gaussian kernels that interact with each other antagonistically. For example, a simple cell with a vertical orientation and a light-dark polarity from left to right pools excitatory inputs from on-center off-surround contrast signals on the left side of the kernel and off-center on-surround signals from the right side of the kernel, and also pools inhibitory inputs from on-center off-surround contrast signals on the right side of the kernel and off-center on-surround signals from the left side of the kernel. Since the output is a rectified version of the sum of the filtered signals, the model simple cell becomes active only when there is an imbalance of luminance with the correct polarity across the oriented axis.

The boundary signals of an object need to be joined together even in cases where the contrast polarity reverses along the border of the object, such as at the edge of a middle gray object on a white-and-black checkerboard background (Grossberg 1994). The model achieves this requirement using model complex cells that pool a pair of light-dark and dark-light simple cell signals of the same orientation at each position. This pooling process is illustrated in Figure 12B. The classical proposal of such a hierarchical combination of simple cell outputs at complex cells (Hubel and Wiesel 1962; Schiller, Finlay & Volman, 1976) is supported by recent experimental data (Alonso & Martinez, 1998; Dresp & Grossberg, 1997; Martinez & Alonso, 2001), a theoretical analysis (Sakai & Tanaka, 2000) and modeling studies (e.g., Gove, Grossberg & Mingolla, 1995; Grossberg & Mingolla, 1985a). By this process, a model complex cell simulates the known complex cell property in V1 of responding to oriented luminance edges without having clear ON/OFF subfield zones (see Mechler & Ringach (2002) for further discussion). Additional feedback interactions are also known to exist (e.g., see Raizada and Grossberg, 2003), but are not needed for present purposes.

2.4 Surface Filling-In

At the filling-in stage, filling-in units first pool signals from multiple scales. Three scales are used: Small-scale and medium-scale contrast signals and large-scale luminance signals. These pooled signals spread during the filling-in process along long-range horizontal connections. The spread is blocked by boundary signals.

The model hereby extends the idea that pooled multiple-scale contrast and luminance signals are filled-in inside boundaries to form a surface percept (Cohen & Grossberg, 1984; Grossberg & Todorović, 1988; Pessoa, Mingolla & Neumann, 1995). This boundary-gated surface filling-in concept has been used to explain many psychophysical data about brightness and color perception and 3D figure-ground perception (Grossberg & Mingolla, 1985b; Grossberg & Kelly, 1999; Grossberg, Hwang & Mingolla, 2002). Consistent with this hypothesis, the

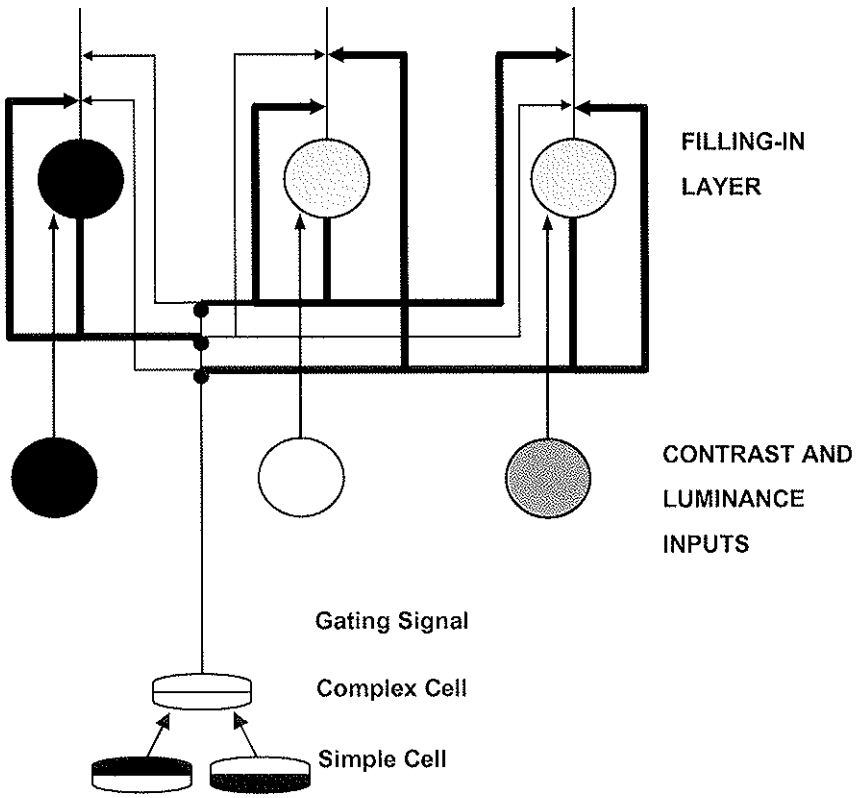

Figure 13. Schematic representation of the parallel filling-in mechanism. In the filling layer, the signals coming from the contrast and luminance units are homogenized within areas defined by luminance boundary signals. The horizontal connections that propagate signals are gated by the gating signals coming from the complex cells. The gated lateral connections have smaller conductances (thin lines) than the other ones (thick ones). The gray levels in the round units represent the activities of them. Just one set of gating signal is shown for clarity.

psychophysical study of surface perception by Paradiso and Nakayama (1991) showed that rapidly formed contour signals may gate the spread of surface signals to form a complete percept of a surface.

The filling-in mechanism utilizes two streams of the What cortical visual pathway: The surface stream runs through the blobs and V2 thin strips to V4; and the boundary stream runs through V1 interblobs and V2 interstrips to V4. These two streams have been proposed to compute complementary properties during visual information processing (Grossberg, 2000). Filling-in in the blind spot is an example of surface filling-in (Komatsu et al., 1996, 2000). Surface representations can be formed early in visual processing even without top-down cognition signals (Kamitani & Shimojo, in press). Sasaki et al. (2001) showed using fMRI that when a human subject perceives a transparent illusory region bounded by illusory contours, the V1 region corresponding to the illusory visual field became active. These data, combined with data about illusory contour representations known to exist in V2, are consistent with the possibility that surface representations may start to form in V2. More direct evidence comes from electrophysiology combined with cortical imaging: Hung et al. (2001) reported that the

Craik-O'Brien-Cornsweet Effect can be detected in V1 and is prevalent in V2. In their experiment, the activities of cells having receptive fields inside the homogeneous surfaces were modulated with cusps at the edge of the surfaces. The large spatial scale needed to fully integrate information across visual space (Angelucci et al., 2002) also marks V2 as a processing stage where surface representations start to get formed. Data concerning border ownership representations in V2 and V4 (Zhou et al., 2000) are also consistent with this conclusion. See Grossberg (1994, 1997) for further discussion.

Figure 13 shows a 1-D illustration of the filling-in model network. The round units on top represent the units in the filling-in layer. The units in the contrast and luminance layer feed their signals to the retinotopically corresponding filling-in units. Then the received signals spread between filling-in cells along long-range horizontal connections with Gaussian receptive fields. Signal propagation is gated by boundary signals (represented by a vertical line in Figure 13) coming from the complex cells (for simplicity just one set of gating units is shown). The gated horizontal connections have smaller conductances (thin horizontal lines) than the other ones (thick horizontal lines). The gray levels of the filling-in cells and the contrast, and luminance input cells represent the level of activation of these cells. The FILLING-IN LAYER illustrates two homogeneous filled-in regions, black and middle gray, separated by a boundary signal, representing two surfaces with different relative reflectances.

2.5 Lightness Anchoring

At the lightness anchoring stage, anchoring units receive the filled-in surface signals, while the activities of the anchoring units are modulated by a feedback signal originating from the anchoring module itself (Figures 9 and 14A).

Anchoring and Blurred Highest Luminance As White (BHLAW) Rule

While the retinal adaptation and contrast calculation stages generate normalized signals, these early processes do not provide output signals that encode an absolute lightness scale. Without an anchoring process, for example, a large whiteboard covering more than half of the visual field may look middle gray (Figure 3), because the early normalizing center-surround processes compute just the relative luminance of the center with the surround as the standard, or anchoring point. This is true for each spatial scale and is also true for the pooled multiple-scale representation. Anchoring rescales these relatively defined surface signals.

To simulate this rescaling process, the model embodies a new anchoring rule, called the Blurred-Highest-Luminance-As-White (BHLAW) rule. As noted in the Introduction, this revision overcomes problems of traditional HLAW rule; namely, a point-like small bright patch on a visual field will be dealt with the same as a large whiteboard occupying most of the visual field (Figure 3). By introducing a spatial Gaussian averaging mechanism into the anchoring

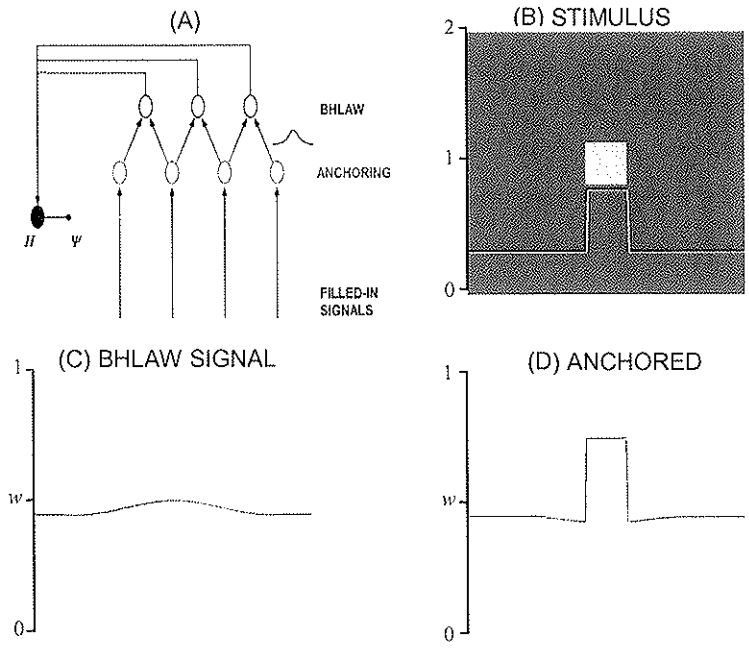

Figure 14. BHLAW rule and Area Effect in a two-field Ganzfeld configuration. (A) Model circuit of lightness anchoring. The activities of the ANCHORING units are locally pooled by BHLAW units to form a blurred version of the ANCHORING signals. The filter used to generate the blurred signals is shown as a bell-shaped figure between the ANCHORING and BHLAW modules. The BHLAW signals are fed to an inhibitory unit *H*. The unit *H* becomes active when any of the BHLAW unit exceeds its threshold set to WHITE and fires. When active, *H* inhibits the tonically active unit Ψ that modulates the activities of ANCHORING units. This circuit allows the activities of ANCHORING units to grow until at least one of the blurred version of anchoring signals, BHLAW, meets the criterion of WHITE. See Appendix A for mathematical details. One thing to notice is that the inhibition by *H* on Ψ lowers but does not completely shut off the activity of Ψ, leaving a chance to the BHLAW signals to go beyond WHITE when the bottom up signal is strong enough, for example, a bright light source of some size. In such a case, even the BHLAW rule will be violated. (B-D), Two-dimensional simulation of two-field Ganzfeld configuration. The curve on each figure represents the activities of the units along the horizontal midline. This convention applies to all the following figures. The scale for the curve is denoted on the left side of each figure. B.STIMULUS shows the input configuration. D.ANCHORED LIGHTNESS shows the area effect corresponding to the one in Figure 4B. Note that the highest activity of the BHLAW module in Figure C is anchored to white (*w*).

process, the model solves this problem and also explains the Gilchrist area effect (Figure 8). Figures 4A and 4B illustrate the model's explanation of the area effect for a two-field Ganzfeld configuration, as in Figure 8. In such a display, there are just two homogeneous surfaces with different luminances, one the target surface, the other the Ganzfeld.

To achieve the anchoring property, the model first makes a blurred version of the anchoring signal, called the BHLAW signal (Figure 14A). The model uses this signal to anchor the highest value of the blurred pattern to white. This rescaling is achieved by using the BHLAW signal to modulate an automatic gain control process, labeled Ψ (Figures 9 and 14A). Gain Ψ multiplicatively rescales the filled-in surface signals. The process *H*, which inhibits Ψ, becomes activated whenever any BHLAW signal exceeds a threshold that determines the value of white

(WHITE in Figures 4A and 4B). Since it is the highest value of the BHLAW signal that the model uses for anchoring, the anchored lightness (ANCHORED LIGHTNESS), or unblurred pattern, will look self-luminous (Figure 4B) in case the area of the highest filled-in activity is not broad enough to span the blurring kernel, because the blurring kernel then averages lower activities as well. As the area of the highest filled-in activity becomes smaller, this mechanism predicts that the background will approach WHITE because of the small difference between the highest and background BHLAW signals (Figure 4A). In such a case, the ANCHORED LIGHTNESS will grow until the highest BHLAW signal equals the anchoring value WHITE, which will also bring the background up close to WHITE. When the area of the highest luminance is larger than the blurring kernel, the highest BHLAW activity will equal the highest ANCHORED LIGHTNESS. Thus there will be no self-luminosity for that region after anchoring (Figure 4A). Figures 14B to 14D show a 2-D simulation of the two-field Ganzfeld configuration. The curve in each figure shows the activities of the cells along the horizontal middle section of the 2-D image. The labels on the left side of each figure indicate the scale of vertical axis for the curve; in particular, *w* denotes white.

3. Results

3.1 Background Light Adaptation

Figure 2C shows light adaptation of model cells to ambient illumination. This shift property simulates the cell recording data of Werblin (1971). The leftmost curve of the shift property at lower values of background luminance corresponds to the physical limit of light adaptation observed in retinal ganglion cells (Barlow & Levick, 1969; Enroth-Cugell & Shapley, 1973a). Over a wide range of background luminances the model obeys the Weber law (Grossberg, 1983). Ambient illumination is removed by divisive intracellular negative feedback signals in the photoreceptors. See Appendix B for stimuli used for this simulation.

3.2 Discounting the Illuminant

Figure 15A shows two light patches on a dark background seen in a gradient of illumination. To generate the input, light patches with the same reflectance and a background with a smaller constant reflectance were multiplied by a gradient of illumination. The curves on Figures 15A and 15B show the input intensities and anchored lightnesses along the horizontal midline, respectively. Figure 15B shows the property of illumination discounting: The light patch on the left is almost as light as the one on the right, unlike the one in Figure 15A. This property comes from the ratio-calculating property of the local contrast units. Figure 15B also shows that, when the gradient of illumination is big enough, the model exhibits a lightness bias where the square patch with higher illumination looks slightly lighter than the one with lower illumination. This

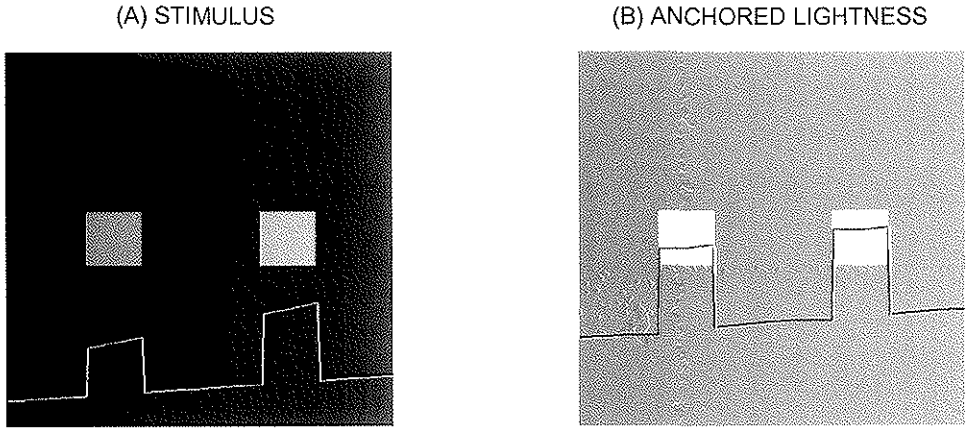

Figure 15. Discounting illuminant. Unevenly illuminated two light patches with identical reflectance (A.STIMULUS) generate a percept that discounts the illumination (B.ANCHORED LIGHTNESS). However, the model also predicts a bit of bias introduced by the illumination gradient. The light patch on the right looks a bit lighter than the left one. The model also picks up the illumination gradient itself using the large scale.

property of the model is due to the influence of the large scale that adds a more veridical representation of the stimuli to percepts. This prediction is supported by the observation that, when subjects are asked to decide the perceived reflectance of surfaces, they always give a higher value to the highly illuminated one than the same one with low illumination. (Gilchrist et. al., 1999, p. 826).

3.3 Simultaneous Contrast

Figure 16 shows a simulation of simultaneous contrast. The two middle gray patches in Figure 16A have identical luminance. In this configuration, small and medium scales calculate local ratio contrasts, and their contribution makes the light square on the dark background look lighter

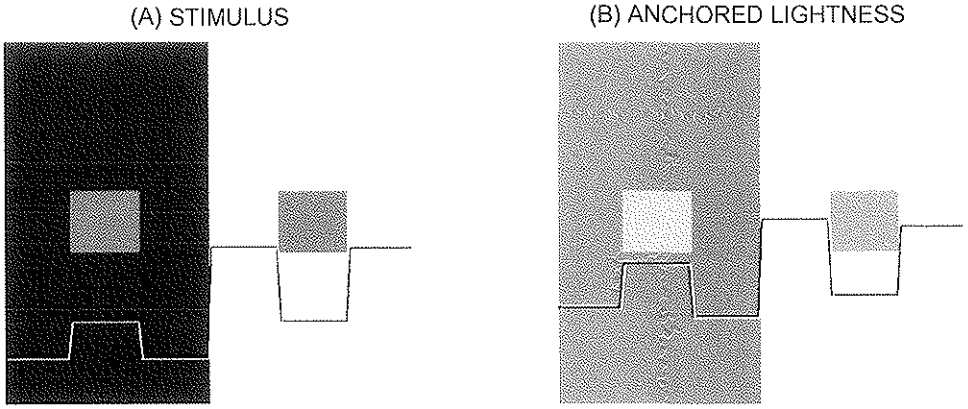

Figure 16. Simultaneous contrast. Two identical square patches on different backgrounds (A.STIMULUS) are perceived differently (B.ANCHORED LIGHTNESS). The one on the dark background looks lighter. Local contrast signals provide the source of this difference.

than the one on the bright background even though they have identical luminance (Figure 16B). Since lightness anchoring just rescales the filled-in multiple-scale signals via BHLAW gain control, the anchoring process does not distort the relative lightnesses of the surfaces.

3.4 Evenly and Unevenly Illuminated Mondrians: Contrast Constancy

Figures 17A and 17B show an evenly illuminated Mondrian and the corresponding prediction of the percept by the model, respectively. A part of the square on the upper left of each figure has been cut and pasted to the square on the bottom right of the figure. Since there is no difference in luminance between the two squares, 17A shows no trace of cut patch at the bottom right square. Figure 17B shows that the square on the top left is perceived to be lighter than the bottom right square. The lightness difference between the two squares in 17B derives from the fact that the square on the right bottom is surrounded by lighter surfaces than the above square. For this reason, the square on the right bottom receives more surround suppression than the square on the

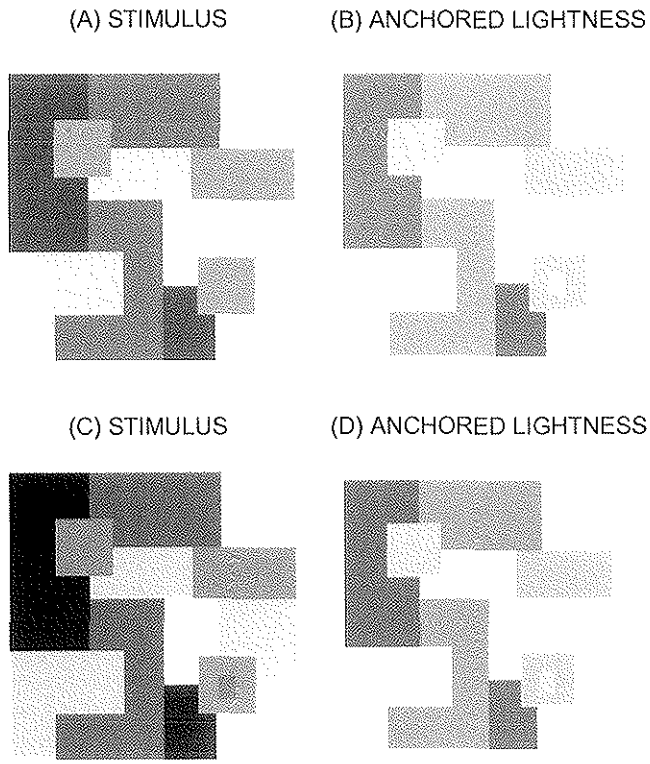

Figure 17. Evenly and unevenly illuminated Mondrians. To facilitate the comparison, a part of the square on the upper left of each figure has been cut and pasted to the square on the bottom right of the figure. (A-B) Evenly illuminated Mondrian. STIMULUS and ANCHORED LIGHTNESS panels show the configuration of an evenly illuminated Mondrian stimulus and the output of the model, respectively. (C-D) Unevenly illuminated Mondrian. The STIMULUS shows the differently illuminated target surfaces because of the illumination gradient. The gradient of illumination is made by a light source located at the bottom-right corner. ANCHORED LIGHTNESS shows the final output of the model. See the text for details.

upper left, which is surrounded by darker surfaces. Figures 17C and 17D show an unevenly illuminated Mondrian and the corresponding percept predicted by the model, respectively. A gradient of illumination from the bottom right to the top left is introduced by a light source located at the bottom right corner. The output of the model (Figure 17D) shows that the square on the upper left looks lighter than the one on the bottom right despite the fact that the luminance at the bottom right is higher. This correct prediction of the reflectances of the squares comes from the fact that the small and medium scales calculate the local contrasts and ignore the global-scale illumination gradient. This contrast constancy calculation by the two scales overrides the prediction by the big scale that picks up the gradient. Grossberg and Todorović (1988) simulated this effect with a single contrast scale.

3.5 Craik-O'Brien-Cornsweet Effect

The model is also capable of explaining the Craik-O'Brien-Cornsweet effect (Cornsweet, 1970), as shown in Figure 18. Figure 18A shows the stimulus with a uniform background luminance with a luminance cusp in the middle. Figure 18B shows the anchored lightness percept in which

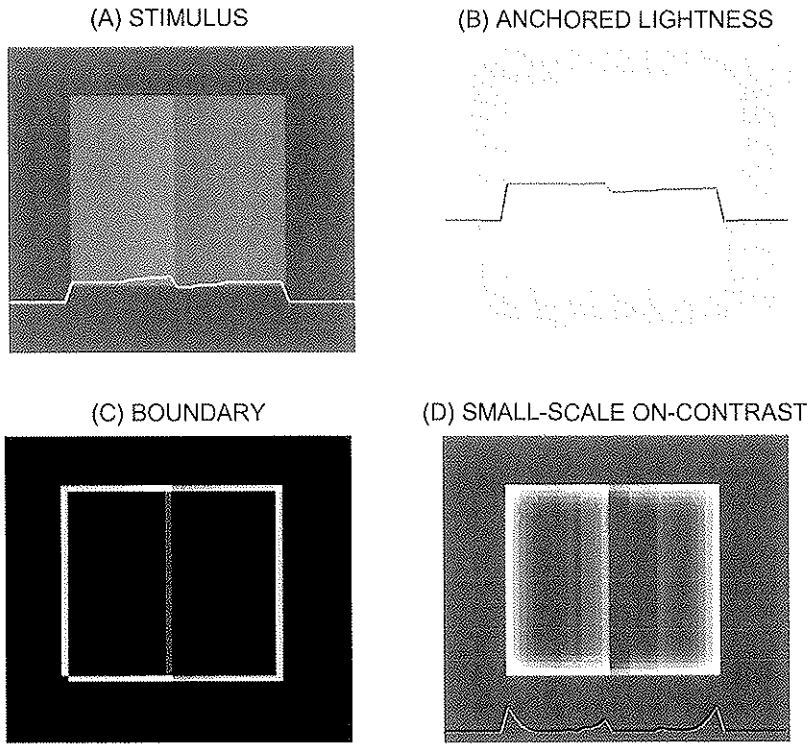

Figure 18. Craik-O'Brien-Cornsweet effect. (A) Two divided identical surfaces with a luminance cusp in the middle. (B) Simulated lightness of the model. The two surfaces are perceived differently. The boundary-gated homogenization of surface signals through a filling-in process makes the surface on the left look slightly lighter than the one on the right. (C) Boundary. (D) Small-scale contrast signals for the two surfaces. Left surface has more activities than the right one explaining the difference at the filled-in surface lightnesses in B.

the left half of the image looks uniformly lighter than the right half. The model explains this illusion using the boundary-gated filling-in process, much as in Grossberg and Todorović (1988). At the filling-in stage, the pooled center-surround contrast signals are flattened within areas defined by boundary signals (Figure 18C). This flattening of signals makes the surface on the left lighter than the one on the right because of the larger contrast activities here (Figure 18D). For the illusion to hold, the area-defining boundaries play a critical role. When no boundaries surround the luminance cusp, the illusion does not happen; see Grossberg and Todorović (1988).

3.6 Double Brilliant Illusion

Bressan (2001) presented a lightness illusion called the Double-Brilliant illusion (Figures 19A and 19B), wherein the diamond that has less contrast around it (Figure 19B) looks lighter than the one having a high contrast around it (Figure 19A) even though both diamonds have the same luminance (Figure 19C). The model ascribes this phenomenon to the gated negative feedback in the retina. Because the permeability of gap junctions in the horizontal cell (HC) syncytium decreases only where there is a sharp luminance edge in the input, the gradual change of luminance around the diamond in Figure 19B does not block the diffusion of signals across the

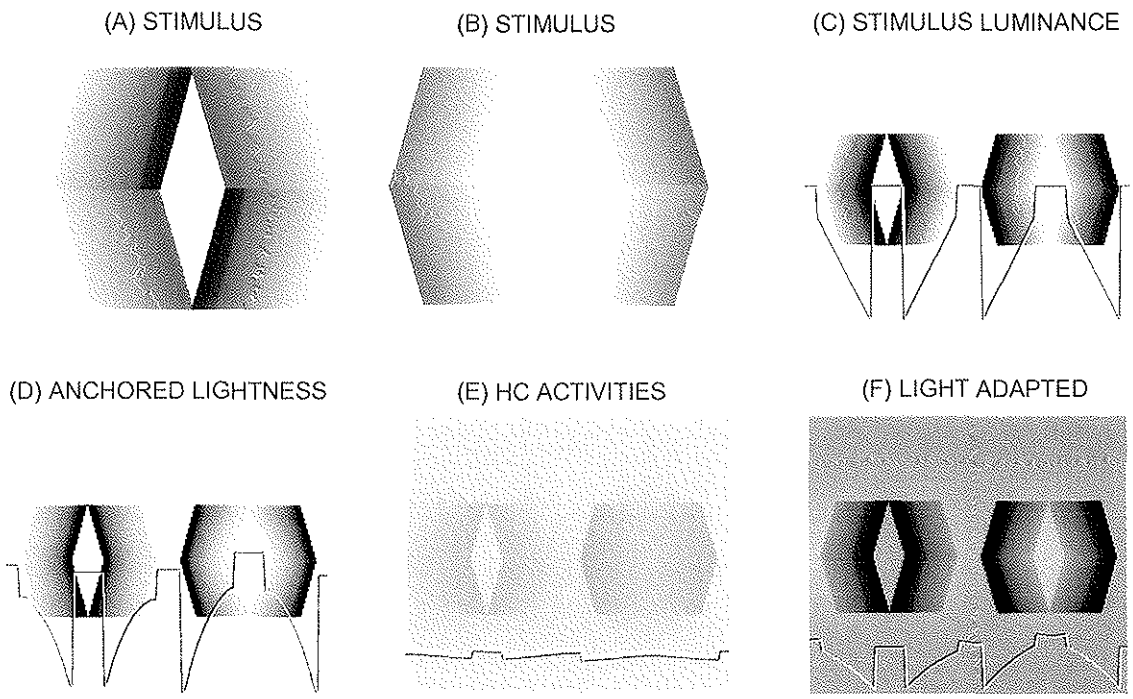

Figure 19. Double Brilliant Illusion. (A-B) Stimuli. A psychophysical experiment shows that the diamond part of the stimulus B looks lighter than that of the stimulus A. (C-D) Stimulus and the output of simulation, respectively. (E-F) Simulated activities of HCs and the steady outputs of photoreceptor inner segments, respectively. See the text for more details. The figures A and B are from Bressan (2000).

HC syncytium. The luminance edges around the diamond in Figure 19A do block the diffusion process and segregate the diamond region from the rest of the figure. This gated-diffusion process is simulated in Figure 19E. The segregated and concentrated high signals shown in the diamond region on the left of 19E suppress the corresponding region of photoreceptor outputs. This results in a less active diamond region on the left in Figure 19F compared to the diamond region on the right. The anchored lightness of the model in Figure 19D reflects this difference and correctly predicts the illusion. This example illustrates that multiple levels of context-sensitive adaptation and recalibration can cooperate to yield lightness percepts. Since the retinal adaptation mechanisms are monocular, dichoptic presentations of different parts of these stimuli to each eye may yield different lightness effects.

3.7 Anchoring Properties

The model explains the four major effects of lightness anchoring (*Articulation, Configuration, Insulation, Area Effect*) as follows:

***Articulation effect*:** The Articulation effect says that, as the display contains more gray surfaces, the range of perceived lightness widens (Figures 5A-5F). One noticeable fact is that even in the two-Mondrian case in Figure 5C, the reflectances of these patches range from black to white covering the full span of reflectance used in the experiment. Thus adding more gray patch does not result in a wider range of reflectance in the experiment. Figure 5G summarizes the model simulation of this effect. As the number of surface patches having different luminances increases in a region, the image contains more high spatial frequencies. In the model, this means that the medium and large spatial scale kernels have less chance to fully activate and suppress the homogeneous area of each patch. Figure 11 illustrates the situation: The divided square luminances on the right cause higher contrast signals in the medium and large-scales compared to the corresponding contrast signals on the left column with a larger square luminance stimulus. The loss of full suppression by each spatial-scale results from the mismatch between the size of the filters and of the patches in the scene. This mismatch at one spatial channel means less suppression, thus more veridical representation for that scale, in turn causing a more veridical percept. The BHLAW process assures that the data remain anchored at white.

***Configuration effect*:** The Configuration effect says that, when a display contains gray surfaces arranged in a Mondrian, a wider range of lightnesses is perceived than when the same gray surfaces are arranged in a luminance staircase. Figures 6E and 6F summarize model simulations. The model explains this effect much as it does the Articulation effect: In the Mondrian configuration, since the intermingled luminance patches are arranged in a more radially compact way, the round-shaped surround kernels in the contrast module are influenced by more luminances of surrounding surfaces compared with the staircase arrangement. This

gives the surround kernels more chance to set the local means (surround activities) to be different from the corresponding center activities. Thus, the increased range of differences between the center and the surround activities results in a bigger range of perceived reflectances for the display. Explained otherwise, if all the adaptation and contrast stage surround activities were the same as their center activities, surround inhibition would drive them all to zero. The radially compact arrangement decreases the distance between different levels of gray patches, thereby inducing stronger lateral inhibition. The dependence of the distance between an inducer and test surfaces has been observed in lightness (Newson, 1958) and brightness experiments (Cole & Diamond, 1971; Fry and Alpern, 1953; Leibowitz et al., 1953), where the darker test surface became lighter with increasing distance from the inducer, an effect interpreted to be due to surround inhibition. Again the BHLAW process anchors the perception of white.

***Insulation effect*:** The Insulation effect of Figure 7 shows that, when the staircase display is insulated by a white surround, the range of its perceived reflectance widens. Figures 7D and 7E show the data and simulation results, respectively. According to the model, a spatial contrast explanation also helps to explain this effect: Insulation of gray surfaces with a white surround causes bigger surround inhibition by the introduced bright insulation on the gray surfaces, making them look darker. This results in an expansion of the range of lightness due to the newly added suppression on dark patches by the surround. Insulation by a black surround, however, may not cause much difference in lightness assessment. This is because the gray surfaces are under illumination 30 times that of the background. Since the gray patches are already not getting much background inhibition, the introduction of black insulation does not significantly change the amount of surround inhibition, thus hardly changing the percept. Once again, the BHLAW process converts these relative lightness activities to an absolute anchored lightness.

***Area effect*:** The Area effect in Figure 8 shows that, in a two-field Ganzfeld situation, as an area other than the area of highest luminance becomes larger than the half of the visual field, its lightness approaches white while the highest luminance area is pushed above white. Figure 8C shows the simulation of this effect. Comparison of data with the simulation shows that the model closely fits the suggested effect. As explained in the Section 2.5, self-luminosity of a small highest luminance area is explained by the BHLAW rule: When the highest luminance area is smaller than the blurring kernel at the anchoring stage, the blurred filled-in surface signals will have shallower highest activities compared to the un-blurred image (Figures 4B). Since the BHLAW mechanism uses the blurred signals to anchor lightness, the anchored lightness of the highest luminance area will look lighter than white. The case in Figure 4B corresponds to the increasing portions of curves in Figures 8B and 8C. The case in Figure 4A corresponds to the flat regions of the curves in Figures 8B and 8C.

4. Discussion

The model developed herein integrates known neuroanatomy, electrophysiology, and psychophysics to clarify how the brain generates a representation of surface lightness. The following discussion analyzes the model's assumptions and limitations.

4.1 Retinal Adaptation

The model simulates the retinal adaptation using two mechanisms. First, at the outer-segment of the photoreceptor, its sensitivity to light is controlled by concentrations of chemicals, such as Ca^{2+} ions, that reflect the photoreceptor's spatio-temporal history of experience of visual stimuli (Koutalos & Yau 1996). Second, a simulated inhibition at the inner-segment of the photoreceptor by the horizontal cells (HCs) was used to approximate HC modulation of glutamate release at the synaptic terminal of the photoreceptor (Fahrenfort et al., 1999; Verweij et al., 1996). This second mechanism instantiates the hypothesis that the communication among HCs through gap junction contributes to spatial contrast adaptation. The permeability of HC gap junctions is known to be modulated by various mechanisms, including neurotransmitters (DeVries & Schwartz, 1989, 1992; McMahon, 1994; Xin & Bloomfield, 2000), and transjunctional voltage (Lu et al., 1999; Spray et al., 1979).

The model assumes that the permeability is governed by an intracellular mechanism, which is in turn controlled by the output of the presynaptic photoreceptor. For example, for two HCs connected by a gap junction, the permeability of the junction decreases as the difference increases between the inputs that the HCs receive from the photoreceptors (Figure 10). Such a model retina can properly rescale inputs that have too much contrast, such as the one in Figure 20A. Figure 20D shows the steady-state HC activities for the input 20A. The dark and light image regions hereby deliver different suppressive feedback signals to the photoreceptors. Figure 20C illustrates the two sensitivity curves of the inner-segments of the photoreceptors caused by two different negative feedback levels of the HC network for the image. Using these two sensitivities, the network can properly rescale the response of the output at the inner-segment of the photoreceptor, which could have mapped to be too low or high in response if it used just one sensitivity, as illustrated in Figure 20B. The rescaled steady-state output of the photoreceptor inner-segments are shown in Figure 20E. The output of the model photoreceptor in Figure 20F shows visible dark and light image regions. Figures 20G, 20H and 20I show a simulation without the HC gating mechanism. The adapted signals in 20H and the output 20I show signal distortion (a halo) along the border of the dark and light parts, and the dark part is less visible. Figures 20J, 20K and 20L show a simulation with no diffusion among HCs. The results show a prominent compression of signals.

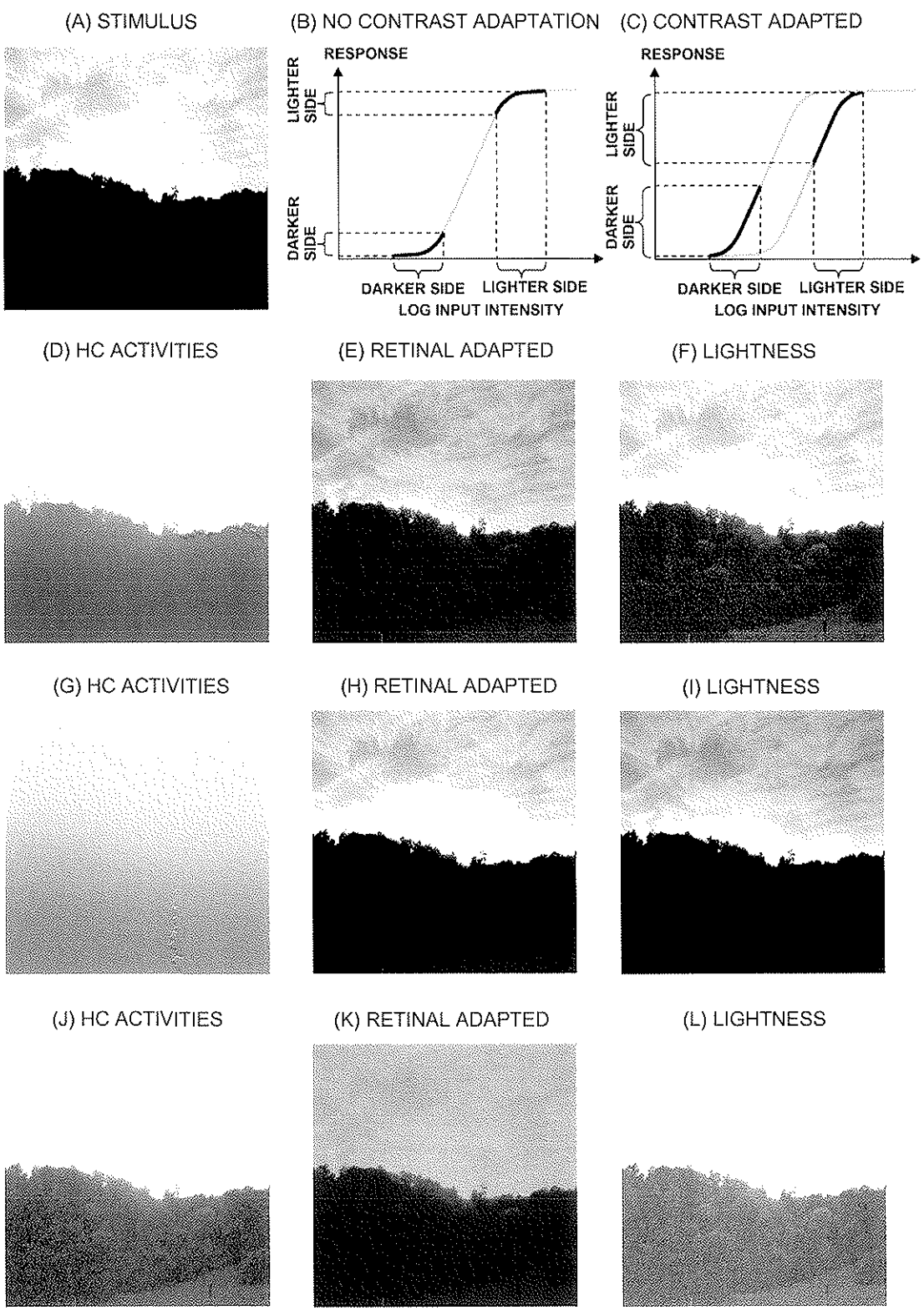
(A) STIMULUS
(B) NO CONTRAST ADAPTATION
(C) CONTRAST ADAPTED
RESPONSE
LIGHTER SIDE
DARKER SIDE
DARKER SIDE
LIGHTER SIDE
LOG INPUT INTENSITY
RESPONSE
LIGHTER SIDE
DARKER SIDE
DARKER SIDE
LIGHTER SIDE
LOG INPUT INTENSITY
(D) HC ACTIVITIES
(E) RETINAL ADAPTED
(F) LIGHTNESS
(G) HC ACTIVITIES
(H) RETINAL ADAPTED
(I) LIGHTNESS
(J) HC ACTIVITIES
(K) RETINAL ADAPTED
(L) LIGHTNESS

Figure 20. Effect of gated diffusion for spatial contrast adaptation of the model. (A) Stimulus. (B) Illustration of retinal sensitivity curve with no contrast adaptation. The signals for the dark part (DARKER SIDE along the abscissa) have been mapped to the very low part of the response axis (DARKER SIDE along the ordinate). The signals for the light part (LIGHTER SIDE along the abscissa) have been mapped to the saturating portion of the curve (LIGHTER SIDE along the ordinate). (C) Illustration of contrast adaptation. With the two different sensitivity curves, the model retina has mapped the widely separated input signals (DARKER SIDE and LIGHTER SIDE along the abscissa) to quite "visible" portions of the response (DARKER SIDE and LIGHTER SIDE along the ordinate). (D) The steady-state activities of HCs at the input A. (E) Retinally adapted signals. Retinal adaptation with gated diffusion at the HC syncytium gives the properly rescaled steady-state output at the inner-segment of the photoreceptor. (F) The final output of the model. (G-I) Simulation with free diffusion among connected HCs. (J-L) Simulation with no diffusion among HCs. See the text for further details

In summary, in addition to the adaptation at the outer-segment of the photoreceptor, which shifts the sensitivity curve of the photoreceptor, the HC negative feedback further shifts photoreceptor sensitivity to be sensitive to the spatial context of input contrasts. This HC feedback is not a compressive process; rather, it shifts the sensitivity curve of the inner-segment of the photoreceptor. See the mathematical details in Appendix A.

HC receptive field size change due to negative feedback between the photoreceptor and the HC was proposed by Kamermans et al. (1996). In his model, Kamermans emphasizes the contribution of the negative feedback on determining the length constant of the HCs. Inclusion of such a mechanism may help further explain the dynamics of retinal adaptation. The model also does not simulate the cone-rod circuitry switch (Mills & Massey, 1995; Ribelayga, Wang & Mangel, 2002) and the pupillary light reflex (Dowling, 1987), which are known to contribute to adaptation. These refinements were not needed to simulate this article's targeted data.

4.2 Multiple-Scale Filtering

The model interprets the neuroanatomy of the retina as the initial source of multiple-scale representation whereby center-surround processes shape the outputs of ganglion cells having diverse receptive field sizes (Masland, 2001; Roska et al., 2000; Werblin, 2001). Direct evidence of multiple-scale representation within V1 includes the fact that cell optimal spatial frequencies gradually increase as their positions move away from blob centers (De Valois & De Valois, 1988; Edwards et al., 1995). Issa et al. (2000) also show gradual changes in cell spatial frequency preferences that conform to the hypercolumn cortical organization in V1. Data about cell responses in LGN, V1 and V2 to uniform surface luminance and color also support the existence of large spatial scales (Bartlett & Doty, 1974; Friedman et al., 2003; Komatsu, 2001; Marrocco, 1972; Papaioannou & White, 1972).

The model hypothesis that cells in the blob stream pool their multiple-scale representations has not yet been directly tested. The pooling of ON and OFF signals, however, is consistent with the finding that the segregation of ON and OFF channels from the retina and LGN, and their projection to layer 4 in V1 (for a review, see Schiller, 1992), is largely lost in the cortex of the ferret (Chapman & Gödecke, 2002).

4.3 Boundary Representation

For simplicity, the model does not implement the boundary completion property of the visual system (Field, Hayes & Hess, 1993; Grossberg & Mingolla, 1985a, 1985b; Grossberg & Raizada, 2000; Kellman, & Shipley, 1991; Raizada & Grossberg, 2001; von der Heydt, Peterhans & Baumgartner 1984). Incorporation of this property into the model would explain more psychophysical data, such as boundary grouping properties like illusory contours (Gove, Grossberg & Mingolla, 1995; Grossberg & Mingolla, 1985a), 3-D figure-ground separation (Grossberg, 1994; Kelly & Grossberg, 2000), and surface noise suppression (Grossberg et al., 1995; Mingolla et al., 1999). Surface noise suppression exploits long-range boundary completion by bipole cells to group noisy pixels into coherent boundaries. Filling-in across noisy surface signals is contained within these boundaries, thus forming a noise-free surface. For figures that do not require significant boundary completion, surface noise suppression can be achieved by the present model's simplified processing. Figure 21D uses a smaller boundary-gating parameter than for Figure 21C.

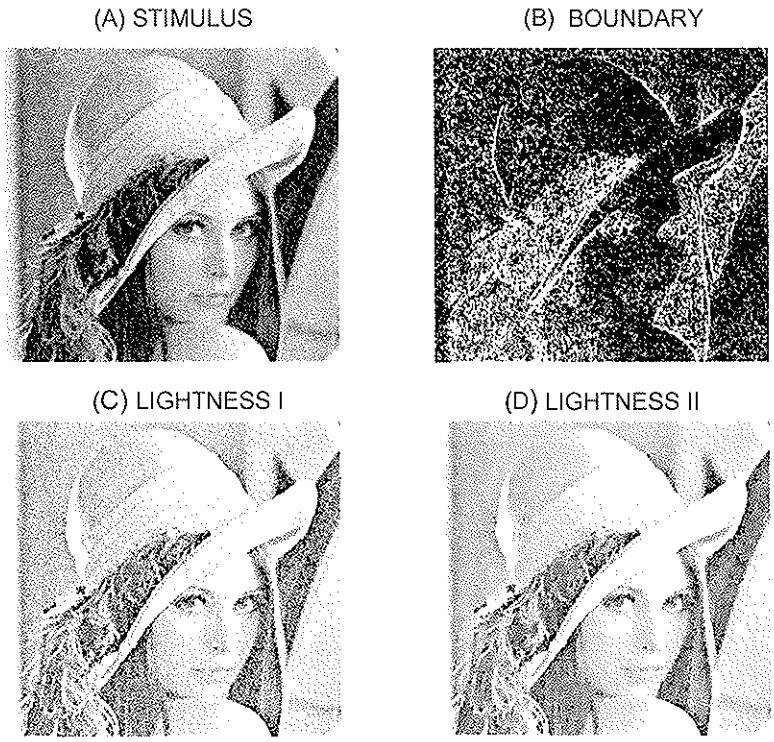

Figure 21. Noise suppression property of the model. (A) Input with Gaussian noise of signal-to-noise ratio of 10 dB. (B) Boundary signals at input A. Despite the disruptive noises, boundary signals still show coherent representation of the edge signals. (C) Output of the model without parameter change. The model does not show much of noise suppression property. (D) Output of the model with a smaller gating parameter (ε = 20). With a smaller gating parameter, the model shows noise suppression property. See the text for further discussion.

4.4 Filling-In

The model proposes a mechanism called Gated Blurring for the filling-in process. Unlike previous filling-in models that use nearest-neighbor diffusion as the cortical mechanism, the current model uses intralaminar propagation via horizontal long-range connections with boundary-gating signals that block signal propagation across luminance edges (Figure 13). This long-range connectivity of the model is consistent with the known horizontal connections in the visual cortices (Angelucci et al., 2002; Gilbert & Wiesel, 1979; Rockland & Lund, 1982; Stettler et al., 2002; Yabuta & Callaway, 1998). The gating mechanism, by selectively allowing communication between only certain connections, can be viewed as a process of dynamic restructuring of neuron receptive fields. One possible mechanism is axo-axonal gating mechanism of the horizontal connections, which is consistent with the report by Kobayashi et al. (2000) of norepinephrine-mediated suppression of horizontal propagation in V1. The mechanism runs at least one hundred times faster than previous nearest-neighbor-based diffusion models, and thus clarifies how filling-in can occur with realistic delays. For example, ten iterations of the non-diffusive filling-in process were used to generate the filled-in image of Craik-O'Brien-Cornsweet effect in Figure 18B. For the long-range diffusive mechanism, 100 iterations were necessary. With the previous diffusion mechanism, which does not have long-range connectivity, about 10,000 iterations were needed to get an output of the same quality. Overall, the model is 100 times faster than the previous models in terms of the filling-in, including the retinal long-range filling-in.

4.5 Lightness Anchoring

The model assumes that lightness anchoring process happens after the filling-in stages in V2 or V4. A recent electrophysiological experiment by MacEvoy and Paradiso (2001) reported lightness constancy in V1. However, their experiment does not provide unequivocal evidence that V1 is the place where anchoring occurs. It demonstrates just one aspect of lightness perception; namely discounting the illuminant, or input normalization, which can be achieved at the adaptation and contrast stages in the model. Even though the model analyses lightness percepts mainly in terms of luminance-based processes, other factors, such as long-range grouping, which take place in V2 (von der Heydt, Peterhans & Baumgartner 1984; Peterhans & von der Heydt, 1989) may also influence the process (see Gilchrist et. al., 1999 for further discussion). The need for extrastriate involvement in the lightness anchoring process also comes from the fact that global integration of information, which is needed for the BHLAW rule, may need a bigger scale of interaction than the one supported by the horizontal connections in V1 (Angelucci et al., 2002). Areas V2 or V4 are probable places for anchoring that satisfy the need for large-scale integration of surface information. V2 provides a rich environment for the

boundary system (interstripes) and luminance and contrast signals (thin stripes) to interact (Roe and Ts'o, 1995) to begin to form surface percepts. The data of Hung et al. (2001) showing a prominent Craik-O'Brien-Cornsweet effect in V2 are also compatible with this assumption.

4.6 Area Effect in Natural Images

The area effect tends to be limited to simple Ganzfeld configurations. Gilchrist and his colleagues (1999. p. 802) note: "Strictly speaking, the rule applies to visual fields composed of only two regions of nonzero luminance. Application of the rule to more complex images remains to be studied." In the model, it is assumed that when the simple Ganzfeld configuration was tested, the visual system of the subject adapted its multiple scales to compensate for the unusually sparse visual cues. In particular, Sections 2.2 and 4.2 noted that the model incorporates multiple spatial scales which suppress signals that are uniform with respect to each scale. Hence, given the sparse contrasts in the Ganzfeld display, the model would be expected to suppress small scales. Multiple scales were not used in the anchoring module, for simplicity. Instead, two different parameter sets were used to explain the area rule: For simple images having just two regions of non-zero luminance (Figure 8), a bigger Gaussian kernel was used. For all the other, more complex, images with smaller regions, a smaller kernel was applied. See Table 1 for parameters. The sizes of the two anchoring kernels were chosen that best fit the sets of data suggested in the Anchoring theory by Gilchrist et al. (1999). Automatic rescaling of the anchoring process will be incorporated when the model fully exploits its multiple scales for purposes of 3-D vision and figure-ground perception; see Grossberg (1994, 1997) for a discussion of how multiple scale are used in 3-D vision.

APPENDIX A: MODEL EQUATIONS

The model implements 2-D simulations on a 200 x 200 grid that represents the whole visual field.

Retinal adaptation

The potential s_{ij} at position (i, j) of the outer segment of the retinal photoreceptor is simulated by the equation:

$$s_{ij}(t) = I_{ij} \cdot z_{ij}(t), \tag{A1}$$

where I_{ij} is the input and $z_{ij}(t)$ is an automatic gain control term simulating negative feedback mediated by Ca^{2+} ions, among others:

$$\frac{dz_{ij}}{dt} = (B_z - z_{ij}) - z_{ij}\left(C_I I_{ij} + C_{\bar{I}}\bar{I}\right), \tag{A2}$$

(cf., Carpenter and Grossberg, 1981; Grossberg 1980). In (A2), parameter B_z is the asymptote which $z_{ij}(t)$ approaches in the absence of input, and term $-z_{ij}(C_I I_{ij} + C_{\bar{I}}\bar{I}_{ij})$ describes the inactivation of z_{ij} by the present input I_{ij} and a spatial average $\bar{I}$ of all inputs that approximates the effect of recent image scanning by sequences of eye movements. The equilibrium response s_{ij} directly follows from (A1) and (A2):

$$s_{ij} = \frac{B_z I_{ij}}{1 + C_I I_{ij} + C_{\bar{I}}\bar{I}}, \tag{A3}$$

The inner segment of the photoreceptor receives the signal s_{ij} from the outer segment and also gets feedback H_{ij} from the horizontal cell (HC) at position (i, j), as in Figure 10. HC modulation of the output of the inner segment of the photoreceptor is modeled by the equation:

$$S_{ij} = \frac{s_{ij}}{B_h \exp\left(H_{ij}\right) \cdot \left(B_s - s_{ij}\right) + 1}, \tag{A4}$$

where B_h is a small constant, and B_s is a constant close to the value (B_z / C_I). When B_s equals the value of (B_z/C_I), perfect shifts of $\log(I_{ij})$ - S_{ij} curve occur with varying H_{ij} (Figure A1A). When B_s deviates from (B_z/ C_I), compression occurs when $B_s > (B_z/ C_I)$ (Figure A1C). Expansion occurs when $B_s < (B_z/ C_I)$ in addition to the shift. Thus to prevent expansion, which would mean excitation by the HC negative feedback, B_s needs to be bigger or equal to (B_z/ C_I). Figure A2 shows the 10-Mondrian Articulation situation (see Figure 5) with two values for B_s, one equals to (B_z/ C_I), and the other to $1.2(B_z/ C_I)$. This simulation demonstrates that the model is robust under this variation. Compare Figure A2 with the graph in Figure 5G.

The equation (A4) can be generalized as follows.

$$S_{ij} = \frac{s_{ij}}{f(H_{ij}) \cdot \left(B_s - s_{ij}\right) + 1}. \tag{A4'}$$

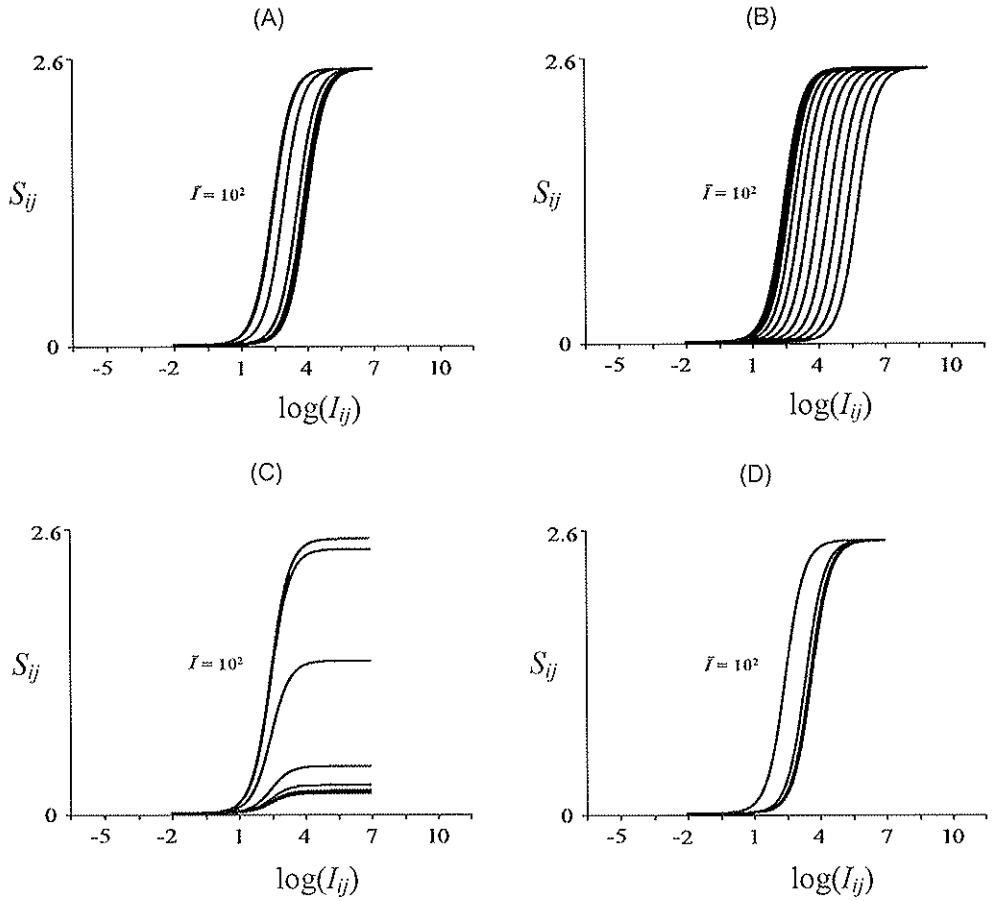

Figure A1. Shift property of spatial contrast adaptation. (A) Shift property of spatial contrast adaptation of the model. The graph shows an example where the $\log(I_{ij})$ - S_{ij} curve smoothly accelerates initially and later decelerates with growing h_{ij}. These curves are generated using the equation A4. These curves and all the following curves in B-D have the same average luminance $\bar{I} = 10^2$. The curves from the left to right have h_{ij} values of 0 to 0.5 with increment 0.1. The same is true for C and D. (B) Shift property with $H_{ij} = h_{ij}$ in placed of the equation A5. The curves show no deceleration. The curves from the left to right have h_{ij} values of 0 to 10 with increment 1. (C) Shift property with no $(B_s - s_{ij})$ term in equation A4. The curves show a prominent compression. (D) Shift property with $f(H_{ij}) = H_{ij}$ in equation A4'. The curves do not have the smooth acceleration shown in graph A.

Many increasing functions $f(H_{ij})$ will generate the shift property of S_{ij} as a function of $\log(I_{ij})$. Function $f(H_{ij}) = B_h \exp(H_{ij})$ was chosen because $\exp(H_{ij})$ makes the sensitivity curve shift in an accelerating manner with increasing H_{ij}, where H_{ij} is the sigmoid output of the HC at (i, j) in response to its potential h_{ij}:

$$H_{ij} = \frac{a_H h_{ij}^2}{b_H^2 + h_{ij}^2}, \qquad \text{(A5)}$$

where a_H and b_H are constants. This bounded function causes the amount of shift to decrease as h_{ij} becomes large. The combination of the initial acceleration by the exponential function in the equation (A4) and the later saturation by the equation (A5) causes the S_{ij} curve to accelerate

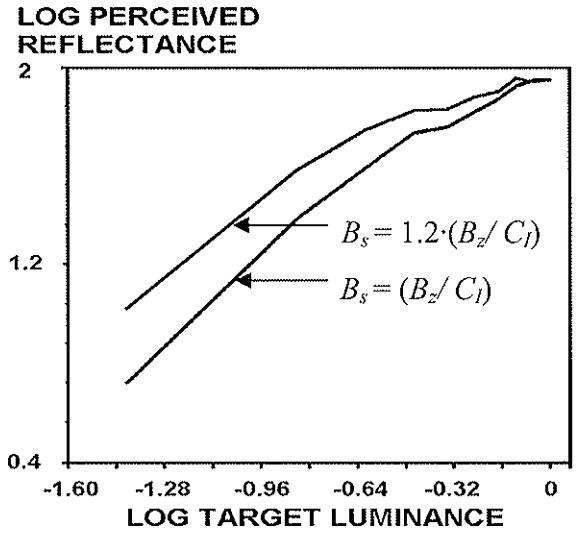

Figure A2. Robustness of the model. The curves show ten-Mondrian Articulation situation with two values for B_s, one (B_z / C_l), the other $1.2(B_z / C_l)$. While the deviation of 20% from the optimal value shows a bit of compression, the overall quality of Articulation effect remains robust. This demonstrates that the model tolerates a fair amount of fluctuation in the value of the parameter.

initially and later decelerate with increasing h_{ij}. Figure (A1A) shows an example of this shift property. The leftmost curve represents the S_{ij} curve with $h_{ij} = 0$; the other curves have h_{ij} values of 0.1, 0.2,... , 0.5, respectively. All these curves have the same average luminance $\bar{I} = 10^2$. The shift property is generated at any average luminance $\bar{I}$. Note that the leftmost curve in Figure (A1A) is the same as the curve with $\bar{I} = 10^2$ in Figure 2C. Figure (A1B) shows what happens when $H_{ij} = h_{ij}$ is used in stead of equation (A5), with all other equations the same; it shows no deceleration. Here, h_{ij} values of 0 to 10 were used with increments of 1. Figure (A1C) shows a situation where the term $(B_s - s_{ij})$ in equation A4 has been replaced by 1; it shows a prominent compression. For this simulation, h_{ij} values of 0 to 0.5 with increments of 0.1 were used. Figure (A1D) shows a situation with $f(H_{ij}) = H_{ij}$ in equation A4'; it does not have the smooth acceleration shown in Figure (A1A). The same h_{ij} values as for Figure (A1C) were used for this simulation.

The potential of an HC connected to its neighbors through gap junctions is defined as follows.

$$\frac{dh_{ij}}{dt} = -h_{ij} + \sum_{(p,q)\in N_{ij}^{H}} P_{pqij}(h_{pq} - h_{ij}) + S_{ij}, \qquad \text{(A6)}$$

where P_{pqij} is the permeability between cells at (i, j) and (p, q); namely,

$$P_{pqij} = \frac{-1}{1 + \exp[-(|S_{ij} - S_{pq}| - \beta_p)/\lambda_p]} + 1 \qquad \text{(A7)}$$

Terms β_p and λ_p in (A7) are constants, and $N^H{}_{ij}$ in (A6) is the neighborhood of size ε_H to which the model HC at (i, j) is connected:

$$N_{ij}^{H} = \left\{(p,q) : \sqrt{(i-p)^2 + (j-q)^2} \le \varepsilon_H \text{ and } (p,q) \ne (i,j)\right\} \tag{A8}$$

Center - Surround Stage

The retinally adapted signal S_{ij} is then processed by small-scale and medium-scale on-center off-surround and off-center on-surround networks. In the following, scale subscripts (e.g., x_s and x_m for small and medium scales, respectively) are omitted for simplicity. An on-center off-surround (ON) network of cell activities $x^+{}_{ij}$ that obey membrane equations is defined as follows:

$$\frac{dx_{ij}^{+}}{dt} = -Ax_{ij}^{+} + (B - x_{ij}^{+})C_{ij} - (x_{ij}^{+} + D)E_{ij}, \tag{A9}$$

where A, B and D are constants. The on-center input obeys:

$$C_{ij} = \left(\sum_{(p,q)\in N_{ij}^{C}} S_{pq} C_{pqij} \right) \frac{W_C}{\sum_{(p,q)\in N_{ij}^{C}} C_{pqij}}, \tag{A10}$$

and the off-surround input obeys:

$$E_{ij} = \left(\sum_{(p,q)\in N_{ij}^{E}} S_{pq} E_{pqij} \right) \frac{W_E}{\sum_{(p,q)\in N_{ij}^{E}} E_{pqij}}, \tag{A11}$$

with the excitatory Gaussian on-center kernel:

$$C_{pqij} = C \exp\left\{ -\frac{(p-i)^2 + (q-j)^2}{\alpha^2} \right\} \tag{A12}$$

and the inhibitory Gaussian off-surround kernel:

$$E_{pqij} = E \exp\left\{ -\frac{(p-i)^2 + (q-j)^2}{\beta^2} \right\}. \tag{A13}$$

Coefficients C and E in (A12) and (A13), which normalize and make the sums of the center and surround kernels the same, are defined by:

$$C = \frac{W_C}{\sum_{(p,q)\in N^C} \exp\left\{ -\frac{p^2 + q^2}{\alpha^2} \right\}} \tag{A14}$$

and

$$E = \frac{W_E}{\sum_{(p,q)\in N^E} \exp\left\{ -\frac{p^2 + q^2}{\beta^2} \right\}}. \tag{A15}$$

Terms α, β, W_C and W_E are constants. $N^C{}_{ij}$ in equation (A10) is the on-center neighborhood to which the cell at (i, j) is connected:

$$N_{ij}^{C} = \left\{(p,q) : \sqrt{(i-p)^2 + (j-q)^2} \le \varepsilon_C \text{ and } 0 \le p \le 199 \text{ and } 0 \le q \le 199\right\}, \qquad \text{(A16)}$$

where ε_C is a constant defining the size of the neighbor. N^C in equation (A14) is the neighbor for the standard center kernel defined as follows.

$$N^{C} = \left\{(p,q) : \sqrt{(i-p)^2 + (j-q)^2} \le \varepsilon_C \right\}. \qquad \text{(A17)}$$

The only difference between $N^C{}_{ij}$ and N^C is that $N^C{}_{ij}$ is constrained by the boundary of the image (200x200), which may cut kernels along the borders, while N^C, which defines the whole kernel, is not. For brevity, the same convention between $N^C{}_{ij}$ and N^C is used for other equations as well. For example, $N^E{}_{ij}$ in equation (A11) is the neighborhood for the surround kernel with a size ε_E with the same form of definition as equation (A16), and its corresponding standard neighbor is N^E with the same form of definition as equation (A17). See Table 1 for parameters.

For each position, the normalizing factors $W_C / \Sigma C_{pqij}$ and $W_E / \Sigma E_{pqij}$ in (A10) and (A11) are constants, mostly just 1, except for the positions along the border of the image. Normalization eliminates unwanted boundary effects created by filters with a fixed kernel size. In case of a center-surround filter, for example, without normalization, halos along the border of the image can occur because of the disinhibition caused by cut kernels there.

The equilibrium activities of (A9) are:

$$x_{ij}^{+} = \frac{BC_{ij} - DE_{ij}}{A + C_{ij} + E_{ij}}. \qquad \text{(A18)}$$

The corresponding equilibrium activities of the off-center on-surround (OFF) network are:

$$x_{ij}^{-} = \frac{BC_{ij}^{-} - DE_{ij}^{-}}{A + C_{ij}^{-} + E_{ij}^{-}} \qquad \text{(A19)}$$

In (A19),

$$C_{ij}^{-} = E_{ij} \qquad \text{(A20)}$$

and

$$E_{ij}^{-} = C_{ij} \qquad \text{(A21)}$$

(Grossberg, Mingolla, and Williamson, 1995). The output signals are rectified versions of x_{ij}^{+} and x_{ij}^{-} :

$$X_{ij}^{+} = \left[x_{ij}^{+}\right]^{+} \qquad \text{(A22)}$$

and

$$X_{ij}^{-} = \left[x_{ij}^{-}\right]^{+}. \qquad \text{(A23)}$$

Luminance signals L_{ij}, which constitute the large-scale of the center-surround process, are defined by:

$$L_{ij} = S_{ij} \qquad \text{(A24)}$$

Through these processes, the initial stage of the model achieves automatic gain control in all its small, medium and large scales.

Boundary System

Simple cell activities are simulated using a network of units having polarized and oriented receptive fields around a gird of pixel units. Figure (A3A) shows pixel units at (i, j) denoted as small filled circles, and eight surrounding numbered positions at (i', j') where pairs of model simple cells with the same orientation but opposite contrast polarity are located. Each simple cell is represented by a half-filled and half-hollow oriented ellipse (Figure A3B). The eight positions are as follows: $(i + 0.5, j)$, $(i + 0.5, j + 0.5)$, $(i, j + 0.5)$, $(i - 0.5, j + 0.5)$, $(i - 0.5, j)$, $(i - 0.5, j - 0.5)$, $(i, j - 0.5)$, $(i + 0.5, j - 0.5)$. A pair of simulated simple cells has one of 4 orientations: $(0, \pi/4, \pi/2, 3\pi/4)$. The even numbered positions have only two $(0, \pi/2)$ orientations; positions 3 and 7 have three orientations $(0, \pi/4, 3\pi/4)$; and positions 1 and 5 have three orientations $(\pi/4, \pi/2, 3\pi/4)$. The responses of simple cells are modeled using medium-scale contrast signals. This simplification was chosen because it gives relative clean edge signals. The outputs from simple cells having light-dark and dark-light luminance polarities in their receptive fields are simulated as follows:

$$s^{LD}_{i'j'k} = \left[\left(L^{+}_{i'j'k} + R^{-}_{i'j'k}\right) - \left(R^{+}_{i'j'k} + L^{-}_{i'j'k}\right)\right]^{+} \tag{A25}$$

$$s^{DL}_{i'j'k} = \left[\left(R^{+}_{i'j'k} + L^{-}_{i'j'k}\right) - \left(L^{+}_{i'j'k} + R^{-}_{i'j'k}\right)\right]^{+}, \tag{A26}$$

where the superscripts LD and DL indicate light-dark and dark-light luminance polarities of the model simple cell receptive fields, respectively, and k denotes the orientation. Activation of a model simple cell left and right sub-receptive fields from ON and OFF channels is modeled as follows:

$$L^{+}_{i'j'k} = \left(\sum_{(p,q)\in N^{B}_{i'j'}} X^{m+}_{pq} G_{pqi'j',kL}\right) \frac{W_B}{\sum_{(p,q)\in N^{B}_{i'j'}} G_{pqi'j',k}} \tag{A27}$$

$$R^{+}_{i'j'k} = \left(\sum_{(p,q)\in N^{B}_{i'j'}} X^{m+}_{pq} G_{pqi'j',kR}\right) \frac{W_B}{\sum_{(p,q)\in N^{B}_{i'j'}} G_{pqi'j',k}} \tag{A28}$$

and

$$L^{-}_{i'j'} = \left(\sum_{(p,q)\in N^{B}_{i'j'}} X^{m-}_{pq} G_{pqi'j',kL}\right) \frac{W_B}{\sum_{(p,q)\in N^{B}_{i'j'}} G_{pqi'j',k}} \tag{A29}$$

$$R^{-}_{i'j'} = \left(\sum_{(p,q)\in N^{B}_{i'j'}} X^{m-}_{pq} G_{pqi'j',kR}\right) \frac{W_B}{\sum_{(p,q)\in N^{B}_{i'j'}} G_{pqi'j',k}}. \tag{A30}$$

Subscripts L and R indicate the two sub-receptive fields for the simple cell with L indicating the left part (to the anticlockwise) of the sub-receptive field, and the R the right part (to the

clockwise) of the sub-receptive field along the axis of the orientation. Constant W_B is the sum of the standard kernel weights of the simple cell:

$$W_B = \sum_{(p,q)\in N^B} G_{pqi'j'k}\,, \tag{A31}$$

At each position, the normalization factor W_B / $\Sigma G_{pqi'j'k}$ is constant, mostly just 1, except for positions along the border of the image where the Gaussian kernel is incomplete. To see the size of the simple cell kernel neighbor, N^B, see ε_B in Table 1.

A pair of oriented Gaussian kernels, indicated as L and R, simulates receptive fields for the simple cell:

$$G_{pqi'j'k,(L\,or\,R)} = \kappa \exp\left\{ -\frac{\left[(p-i')\cos(\pi k/4)+(q-j')\sin(\pi k/4)\right]^2}{\gamma_h^2} - \frac{\left[-(p-i')\sin(\pi k/4)+(q-j')\cos(\pi k/4)+Shift_{(L\,or\,R)}\right]^2}{\gamma_v^2} \right\}, \tag{A32}$$

where $Shift_{(L)}$ and $Shift_{(R)}$, which shift the sub-receptive fields orthogonal to the axis of orientation, are constants $-\gamma_v$ and γ_v, respectively; κ is a constant. k is one of the four numbers (1, 2, 3, 4) that sets the orientation; and γ_h and γ_v are constants that define the widths of the kernel along and across the axis of orientation, respectively.

The model complex cells are also located at the eight (i', j') positions, and have oriented receptive fields, as illustrated in Figure (A3C). The model complex cell of orientation k at (i', j') pools the outputs of a pair of simple cells as follows:

$$z_{i'j'k} = s^{LD}_{i'j'k} + s^{DL}_{i'j'k}\,. \tag{A33}$$

This cell potential goes through an activation function:

$$Z_{i'j'k} = f(z_{i'j'k})\,, \tag{A34}$$

where

$$f(x) = \frac{a_B x^{1.7}}{b_B^2 + x^{1.7}}\,. \tag{A35}$$

The parameter 1.7 of the power of x was in (A35) used that gave the optimal strength of the boundary signals across simulations. The complex cell gates any horizontal connections that cross its gating field. The effective gating strength at a point (x, y) along a passing horizontal connection is the product of the gating weight ($G^c_{xyi'j'k}$) at the point and the activation of the gating complex cell at (i', j') ($Z_{i'j'k}$):

$$Z'_{xyi'j'k} = G^c_{xyi'j'k} Z_{i'j'k}\,, \tag{A36}$$

where x, y are continuous variables. The Gaussian kernel of the gating field, which represents the spatial spread of gating weight of complex cell axons at points (x, y) along the line (i, j) - (p, q), is defined as follows:

$$G^{c}_{xyi'j'k} = \exp\left\{ -\frac{[(x-i')\cos(\pi k/4)+(y-j')\sin(\pi k/4)]^2}{\gamma^2_{ch}} - \frac{[-(x-i')\sin(\pi k/4)+(y-j')\cos(\pi k/4)]^2}{\gamma^2_{cv}} \right\}, \qquad \text{(A37)}$$

Figures (A3D) and (A3E) show an example of the complex cell gating mechanism for a given input. For a given complex gating field, it is assumed that the gating occurs at just one point for each crossing connection. The gating point (x, y), which lies along the line (i, j) - (p, q), is chosen that gives the maximum value of equation (A37). In the simulation, 10 equidistance points along the cross-section between the ellipse and the crossing line (i, j) - (p, q) were examined to find the approximate inflection (maximum) point as shown in Figure (A3F). The size of each dot in the figure represents the value $G^{c}_{xyi'j'k}$ of equation (A37) for each examined point.

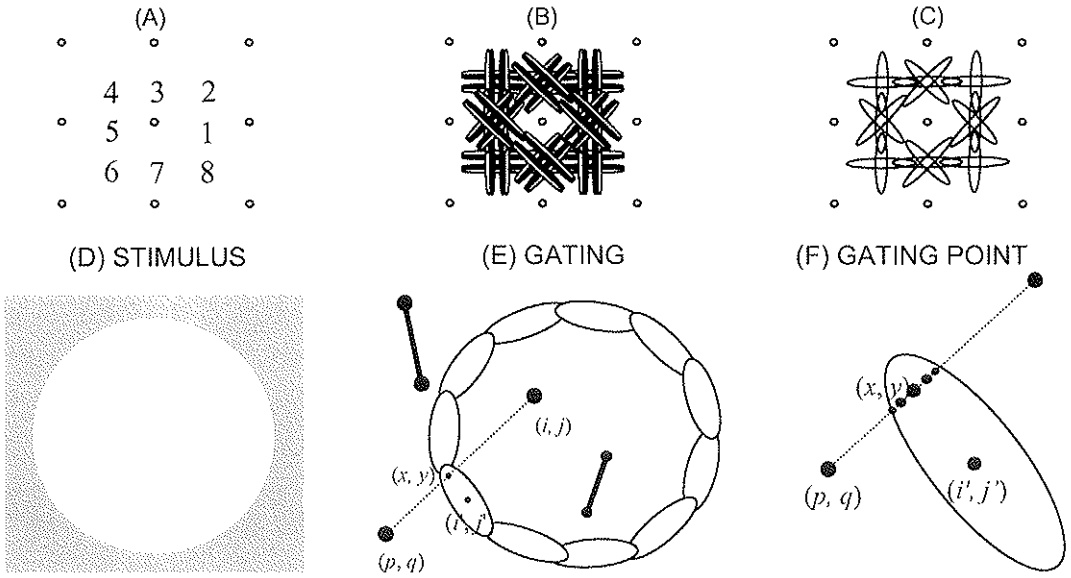

Figure A3. Model boundary system and gating mechanism. (A) Relative positions of model simple and complex cells to pixel points. The model simple and complex cells are poisoned between the pixel points. For example, for a given pixel in the middle (the small gray filled circle in the middle), there are eight surrounding positions (1 through 8) where simple and complex cells are placed. (B) Configuration of simple cell network around a pixel unit in the middle. (C) Gating field of complex cells around the pixel unit. Just one set of pixel-complex and simple cell relationship is shown for clarity. The same pixel-complex and simple cell relationship applies to other pixels. (D) Example of a stimulus. (E) Illustration of gating mechanism for stimulus D. It illustrates the resulting activations of gating components with the input in figure D. The activated complex cells that surround the disk area gate any connections crossing their gating fields represented as ellipses. The connection between (i, j) and (p, q) is gated (the doted line) by a gating signal at (x, y) in the gating field of the complex cell centered at (i', j'). The other connections are not gated, being allowed to have high conductances (solid lines). For the purpose of illustration, more orientations are shown than the four orientations used for the simulations. (F) Position of the gating point. The figure shows the blown up part of the gated part of the connection in the figure E. In the simulation, 10 equidistance points (5 of them are shown for clarity) along the cross-section between the ellipse and the crossing line (i, j) - (p, q) were examined to find the approximate inflection (maximum) point. The size of each dot represents the value $G^{c}_{xyi'j'k}$ of equation (A37) for each examined point.

Filling-in

Cortical filling-in is driven by the inputs M_{ij} which are the pooled luminance and contrast signals as follows:

$$M_{ij} = \left[w_s \left(X_{ij}^{s+} - X_{ij}^{s-} \right) + w_m \left(X_{ij}^{m+} - X_{ij}^{m-} \right) + w_l L_{ij} + b_M \right]^+ , \qquad \text{(A38)}$$

where w_s, w_m, w_l, are weighting constants, and b_M is a tonic bias term. Either of two versions of the filling-in process yield equivalent simulations of the targeted data. A long-range diffusion process, much as in the retinal HC diffusion in (A6), works well with activities F_{ij} instead of the activities h_{ij} in (A6), and inputs M_{ij} instead of the inputs S_{ij} in (A6). This long-range diffusion runs 100 times faster than previous nearest-neighbor diffusions for filling-in. In addition, the conductance P_{pqij} are divisively gated by activated complex cells along its path. They are defined by:

$$P_{pqij} = \frac{\delta \exp\left[-\left((i-p)^2 + (j-q)^2 \right) / \sigma^2 \right]}{\prod_{i'j'k} \left(1 + \varepsilon Z_{i'j'k}^{'} \right)} , \qquad \text{(A39)}$$

where σ, δ and ε are constants. The numerator of (A39) describes the strengths of horizontal connections, assumed to have a Gaussian distribution, such that longer connections have smaller strengths.

Alternatively, a long-range propagation process that does not require diffusion, but is normalized in a different way, generates essentially identical simulations, which are the ones that are shown in this article. This process runs 1000 times faster than nearest-neighbor diffusion processes. The first step of the filling-in is to activate the filling-in units with the pooled multiple-scale input signals M_{ij}:

$$F_{ij} = M_{ij} . \qquad \text{(A40)}$$

Here, the filling-in activity F_{ij} (t+1) equals:

$$F_{ij}(t+1) = \left(\sum_{(p,q) \in N_{ij}^F} F_{pq}(t) P_{pqij} \right) \frac{W_F}{\sum_{(p,q) \in N_{ij}^F} P_{pqij}} , \qquad \text{(A41)}$$

where the conductance P_{pqij} shares the same form of equation (A39) with different parameters (see Table 1). The constant W_F in (A41) is a sum of conductances defined as follows:

$$W_F = \sum_{(p,q) \in N^F} \frac{\delta \exp\left[-\left(i^2 + j^2 \right) / \sigma_F^2 \right]}{\prod \left(1 + 0 \right)} . \qquad \text{(A42)}$$

Since W_F is constant, the constant δ for a fixed σ is calculated as follows:

$$\delta = \frac{W_F}{\sum_{(p,q) \in N^F} \exp\left\{ -\left(i^2 + j^2 \right) / \sigma^2 \right\}} . \qquad \text{(A43)}$$

The size of the filling-in neighborhood N^F is determined by parameter ε_F in Table 1. Equation (A41) assumes that the filling-in unit can normalize its conductances. The normalizing factor

$W_F/\Sigma P_{pqij}$ affects the conductance in two ways. First, at the border of the image, the incomplete kernels get normalized to have the same size as W_F. Second, normalization compensates for the overall lost conductance caused by gating (division by the denominator in equation (A39)). By this normalization process, the sum of the effective conductances equals:

$$W_F = \sum_{pq}\left(P_{pqij}\frac{W_F}{\sum_{pq} P_{pqij}} \right). \tag{A44}$$

For example, if half of the input connections were totally blocked by gating signals, the unit would try to increase the effective input flow by doubling the efficacy of the remaining connections, keeping the sum of all the incoming conductances the same. Ten iterations of equation (A41) gives satisfactory filled-in results.

Lightness Anchoring

At the anchoring stage, the filled-in surface activity F_{ij} becomes anchored into the activity A_{ij} using the following equation:

$$\frac{dA_{ij}}{dt} = -B_A A_{ij} + \Psi\left(C_A - A_{ij}\right)F_{ij}, \tag{A45}$$

where B_A and C_A are constants. The tonic gain control signal Ψ, which modulates all the anchoring activities A_{ij}, uses the following equation.

$$\frac{d\Psi}{dt} = \tau_\Psi\left\{-\Psi + \left(B_\Psi - \Psi\right)T_\Psi - \Psi H\right\}. \tag{A46}$$

The term τ_ψ is a time constant that determines the speed of integration of equation (A46). The term $-\Psi$ is a leakage component. The next term $(B_\psi - \Psi)T_\psi$ is an excitatory component that drives the gain control signal Ψ toward its maximum B_ψ until the inhibitory component ΨH kicks in due to the activation of the suppressive signal H, which is defined as follows:

$$\frac{dH}{dt} = \tau_H\left\{-H + \left(\varphi - H\right)\sum_{ij} B_{ij}\right\}, \tag{A47}$$

where τ_H is a time constant. Using the equation (A47), the suppressive signal H quickly becomes activated and suppresses the gain control activity Ψ whenever there is an activated output cell at the BHLAW module, which signals the anchoring of blurred "highest luminance" to white. The output of the BHLAW module B_{ij} is defined as follows:

$$B_{ij} = f^B\left(b_{ij}\right), \tag{A48}$$

where the signal function $f^B(x)$ is a steep sigmoid:

$$f^B(x) = \frac{x^m}{\varpi^m + x^m}, \tag{A49}$$

where m and ϖ are constants; see Table 1. Function b_{ij} in (A48) is a blurred version of the anchoring signal A_{ij}:

$$b_{ij} = \sum_{(p,q)\in N_{ij}^{A}} G_{pqij}^{A} A_{pq}, \tag{A50}$$

where the blurring Gaussian anchoring kernel is defined by:

$$G_{pqij}^{A} = G^{A} \exp\left\{-\frac{(p-i)^2 + (q-j)^2}{\zeta_A^2}\right\} \frac{W_A}{\sum_{(p,q)\in N_{ij}^{A}} G_{pqij}^{A}}, \tag{A51}$$

where constant

$$G^{A} = \frac{W_A}{\sum_{(p,q)\in N^{A}} \exp\left\{-\frac{p^2+q^2}{\zeta_A^2}\right\}}, \tag{A52}$$

and W_A and ζ_A are constants. The size of the blurring neighborhood N^A is determined by paramenter ε_A in Table 1. When m in equation (A49) is large, H approximates a step function

$$\begin{cases} H = \varphi & \text{whenever any } \; b_{ij} \geq \varpi \\ H = 0 & \text{otherwise,} \end{cases} \tag{A53}$$

where φ is a constant. In the simulation, equation (A53) was used in place of equations (A47) to (A49).

APPENDIX B

To generate the stimuli with different background luminance (Figure 2C), the following formula was used:

$$I_{ij} = \rho_{ij} E_{ij}, \tag{B1}$$

where I_{ij} is the luminance at point (i, j), ρ_{ij} is the reflectance at point (i, j), and E_{ij} is the illumination on point (i, j) (Hurlbert, 1989). For a given stimulus, E_{ij} was uniform across the image. For practical purposes, ρ_{ij} in equation (B1) was replaced by the luminance at point (i, j) of the original image. This situation is roughly equivalent to a viewing situation where a picture is exposed to uniform background illumination. The range of ρ_{ij} was chosen to be –4 to 5 in log-scale for a fixed illumination level to examine the full dynamic profile of the shift property. See Figure 2C for the values of illumination E_{ij} used for the simulations.

Table 1

Names	Symbols	Values
Upper bound of gain control at photoreceptor	B_z	500
Small-time scale input contribution rate for gain control	C_l	200
Large-time scale input contribution rate for gain control	C_l	600
	B_h	0.04
	B_s	(B_z/C_l)
	a_H	6
	b_H	0.1
Shift of permeability of HC gap junction	β_p	0.08
Steepness of permeability of HC gap junction	λ_p	0.01
Size of connected neighbor for horizontal cell	ε_H	8
Activation decay	A	0.5
Depolarization constant	B	1
Hyperpolarization constant	D	1
Center spatial scale for the center-surround stage	α	0.2
Surround spatial scales, small, medium	β	3 (for small scale), 14 (for medium scale)
	κ	4
Vertical, horizontal widths of the ON, OFF elliptic simple cell receptive fields	γ_v, γ_h	0.1, $5\gamma_v$,
The shift of the centers of the ON, OFF elliptic simple cell receptive fields	$Shift_{(L)}$, $Shift_{(R)}$	$-\gamma_v$, γ_v
	a_B	0.7
	b_B	0.15
Vertical/horizontal width of the complex cell's gating field	γ_{cv}, γ_{ch}	0.3, 0.7
Small, Medium, Large Scale Weight	w_s , w_m, w_l	0.25, 0.25, 0.5
Baseline bias of multiple-scale input	b_M	0.01
Spatial constant of the cable of the filling-in unit	σ	30
	ε	100

Names	Symbols	Values
Decay rate for Anchoring	B_A	1
Depolarization constant for Anchoring	C_A	10
Time constant of modulatory unit of anchoring	τ_Ψ	0.01
Depolarization constant of modulatory unit of anchoring	B_Ψ	1.3
Recharge rate of tonic activity	T_Ψ	1
	m	100
White	ϖ	0.5
Hyperpolarization constant for gain control	φ	8
Spatial scale for Anchoring	ζ_A	100 (for the area rule), 4 (for the others)
Size of connection range for the center of center-surround unit	ε_C	6 (for small scale), 28 (for medium scale)
Size of connection range for the surround of center-surround unit	ε_E	6 (for small scale), 28 (for medium scale)
Size of connection range for the half kernel of simple cell	ε_B	3
Size of connection range for the blurring kernel of Anchoring	ε_A	100 (for the area rule), 4 (for the others)
Size of connection range for the filling-in unit	ε_F	8
Sizes of various standard kernels	W_C, W_E, W_B, W_A, W_F	0.6, 0.6, 4, 1, 1

References

Adams, M.M., Hof, P.R., Gattass, R., Webster, M.J., & Ungerleider, L.G. (2000). Visual cortical projections and chemoarchitecture of macaque monkey pulvinar. *Journal of Comparative Neurology*, **419**, 377-393.

Adelson, E.H., & Pentland, A.P. (1996). The perception of shading and reflectance. In D.C. Knill & W. Richards (Eds.), *Perception as Bayesian inference* (pp. 409-423). New York: Cambridge University Press.

Adelson, E.H. (2000). Lightness perception and lightness illusions. In *The Cognitive Neurosciences*, Ed., M. Gazzaniga (Cambridge, MA: MIT Press), pp 339-351.

Alonso, J.M., & Martinez, L.M. (1998). Functional connectivity between simple cells and complex cells in cat striate cortex. *Nature Neuroscience*, **1**, 395-403.

Alonso, J.M., Usrey, W.M., & Reid, R.C. (2001). Rules of connectivity between geniculate cells and simple cells in cat primary visual cortex. *Journal of Neuroscience*, **21**, 4002-4015.

Anderson, B.L. (1997). A theory of illusory lightness and transparency in monocular and binocular images: the role of contour junctions. *Perception*, **26**, 419-453.

Angelucci, A., Levitt, J.B., Walton, E.J., Hupé, J.M., Bullier, J., & Lund, J.S. (2002). Circuits for local and global signal integration in primary visual cortex. *Journal of Neuroscience*, **22**, 8633-8646.

Arend, L.E. (1990). Perceived lightness, but not brightness of achromatic surfaces depends on perceived depth information. *Perception & Psychophysics*, **48**, 82-90.

Arend, L.E. (1993). Mesopic lightness, brightness, and brightness contrast. *Perception & Psychophysics*, **54**, 469-476.

Arend, L.E. (1994). Surface colors, illumination, and surface geometry: Intrinsic-image models of human color perception. In A. Gilchrist (Ed.), *Lightness, brightness, and transparency* (pp. 159-213). Hillsdale, NJ: Erlbaum.

Arend, L.E., & Reeves, A. (1986). Simultaneous color constancy. *Journal of the Optical Society America*, **3**, 1743-1751.

Arend, L.E., & Spehar, B. (1993a). Lightness, brightness, and brightness contrast: 1. Illuminance variation. *Perception & Psychophysics*, **54**, 446-456.

Arend, L.E., & Spehar, B. (1993b). Lightness, brightness, and brightness contrast: 2. Reflectance variation. *Perception & Psychophysics*, **54**, 457-468.

Arrington, K.F. (1994). The temporal dynamics of brightness filling-in. *Vision Research*, **24**, 3371-3387.

Baccus, S.A., & Meister, M. (2002). Fast and slow contrast adaptation in retinal circuitry. *Neuron*, **36**, 909-919.

Barlow, H.B. (1953). Summation and inhibition in the frog's retina. *Journal of Physiology (London)*, **119**, 69-88.

Barlow, H.B., & Levick, W.R. (1969). Three factors limiting the reliable detection of light by retinal ganglion cells of the cat. *Journal of Physiology*, **200**, 1-24.

Barlow, R.B., Snodderly, D.M., & Swadlow, H.A. (1978). Intensity coding in primate visual system. *Experimental Brain Research*, **31**, 163-177.

Bartlett, J.R., & Doty, R.W. (1974). Response of units in striate cortex of squirrel monkeys to visual and electrical stimuli. *Journal of Neurophysiology*, **37**, 621-641.

Baylor, D.A., Hodgkin, A.L., Lamb, T.D. (1974a). The electrical response of turtle cones to flashes and steps of light. *Journal of Physiology*, **242**, 685-727.

Baylor, D.A., Hodgkin, A.L., Lamb, T.D. (1974b). Reconstruction of the electrical responses of turtle cones to flashes and steps of light. *Journal of Physiology*, **242**, 759-791.

Benda, J., Bock, R., Rujan, P., & Ammermuller, J. (2001). Asymmetrical dynamics of voltage spread in retinal horizontal cell networks. *Visulal Neuroscience*, **18**, 835-848.

Bickford, M.E., Günlük, A.E., Guido, W., & Sherman, S.M. (1993). Evidence that cholinergic axons from the parabrachial region of the brainstem are the exclusive source of nitric oxide in the lateral geniculate nucleus of the cat. *Journal of Comparative Neurology*, **334**, 410-430.

Bloomfield, S.A., Xin, D., & Persky, S.E. (1995). A comparison of receptive field and tracer coupling size of horizontal cells in the rabbit retina. *Visual Neuroscience*, **12**, 985-999.

Bonato F, & Cataliotti J. (2000). The effects of figure/ground, perceived area, and target saliency on the luminosity threshold. *Perception & Psychophysics*, **62**, 341-349.

Bonato F, & Gilchrist A.L. (1994). The perception of luminosity on different backgrounds and in different illuminations. *Perception*, **23**, 991-1006.

Bonato F, & Gilchrist A.L. (1999). Perceived area and the luminosity threshold. *Perception & Psychophysics*, **61**, 786-797.

Bressan, P. (2001), Explaining lightness illusions. *Perception*, **30**, 1031-1046.

Bressan, P., Mingolla, E., Spillmann, L., & Watanabe, T. (1997). Neon color spreading: a review. *Perception*, **26**, 1353-1366.

Brown, S.P., & Masland, R.H. (2001). Spatial scale and cellular substrate of contrast adaptation by retinal ganglion cells. *Nature Neuroscience*, **4**, 44-51.

Budd, J.M. (1998). Extrastriate feedback to primary visual cortex in primates: a quantitative analysis of connectivity. *Proceedings of The Royal Society of London Series B-Biological Sciences*, **265**, 1037-1044.

Bullier, J., & Henry, G.H. (1979). Laminar distribution of first-order neurons and afferent terminals in cat striate cortex. *Journal of Neurophysiology*, **42**, 1271-1281.

Bullier, J., Hupé, J.M., James, A.C., & Girard, P. (1996). Functional interactions between areas V1 and V2 in the monkey. *Journal of Physiology Paris*, **90**, 217-220.

Bullier, J., Hupé, J.M., James, A.C., & Girard, P. (2001). The role of feedback connections in shaping the responses of visual cortical neurons. *Progress in Brain Research*, **134**, 193-204.

Burkhardt, D.A. (1994). Light adaptation and photopigment bleaching in cone photoreceptors *in situ* in the retina of the turtle. *Journal of Neuroscience*, **14**, 1091-1105.

Calvert, P.D., Govardovskii, V.I., Arshavsky, V.Y., & Makino, C.L. (2002). Two temporal phases of light adaptation in retinal rods. *Journal of General Physiology*, **119**, 129-145.

Callaway, E.M. (1998). Local circuits in primary visual cortex of the macaque monkey. *Annual Review of Neuroscience,* **21**, 47-74.

Caputo, G. (1998). Texture brightness filling-in. *Vision Research*, **38**, 841-851.

Carpenter G., & Grossberg, S. (1981). Adaptation and transmitter gating in vertebrate photoreceptors. *Journal of Theoretical Neurobiology*, **1**, 1-42.

Cataliotti, J., & Gilchrist, A. (1995). Local and global processes in surface lightness perception. *Perception & Psychophysics*, **57**, 125-135.

Chapman, B., & Gödecke, I. (2002). No ON-OFF maps in supragranular layers of ferret visual cortex. *Journal of Neurophysiology*, **88**, 2163-2166.

Cohen, M.A., & Grossberg, S. (1984). Neural dynamics of brightness perception: features, boundaries, diffusion, and resonance. *Perception & Psychophysics*, **36**, 428-456.

Cole, R.E., & Diamond, A.L., (1971). Amount of surround and test inducing separation in simultaneous brightness contrast. *Perception & Psychophysics*, **9**, 125-128.

Cook, P.B., & McReynolds, J.S. (1998). Lateral inhibition in the inner retina is important for spatial tuning of ganglion cells. *Nature Neuroscience*, **1**, 714-719.

Cornsweet, T.N. (1970). Visual perception. New York: Academic Press.

Dacheux, R.F., & Raviola, E. (1982). Horizontal cells in the retina of the rabbit. *Journal of Neuroscience*, **2**, 1486-1493.

Davey, M.P., Maddess, T., & Srinivasan, M.V., (1998). The spatiotemporal properties of the Craik-O'Brien-Cornsweet effect are consistent with 'filling-in'. *Vision Research*, **38**, 2037-2046.

Davidson, M., & Whiteside, J.A. (1971). Human brightness perception near sharp contours. *Journal of the Optical Society America*, **61**, 530-536.

Demb, J.B. (2002). Multiple mechanisms for contrast adaptation in the retina. *Neuron*, **36**, 781-783.

De Valois, R.L., Cottaris, N.P., Mahon, L.E., Elfar, S.D., & Wilson, J.A., (2000). Spatial and temporal receptive fields of geniculate and cortical cells and directional selectivity. *Vision Research*, **40**, 3685-3702.

De Valois, R.L., & De Valois, K.K. (1988). *Spatial vision*. New York: Oxford University Press.

DeVries, S.H., & Schwartz, E.A. (1989). Modulation of an electrical synapse between solitary pairs of catfish horizontal cells by dopamine and second messengers. *Journal of Physiology*. **414**, 351-375.

DeVries, S.H., & Schwartz, E.A. (1992). Hemi-gap-junction channels in solitary horizontal cells of the catfish retina. *Journal of Physiology*. **445**, 201-230.

Dolan, R.P., & Schiller, P.H. (1994). Effects of ON channel blockade with 2-amino-4-phosphonobutyrate (APB) on brightness and contrast perception in monkeys. *Visual Neuroscience*, **11**, 23-32.

Dowling, J.E. (1987). The Retina: An approachable part of the brain. (Cambridge, MA; Harvard University Press).

Dresp, B., & Grossberg, S. (1997). Contour integration across polarities and spatial gaps: from local contrast filtering to global grouping. *Vision Research*, **37**, 913-924.

Dubin, M.W., & Cleland, B.G. (1977). Organization of visual inputs to interneurons of lateral geniculate nucleus of the cat. *Journal of Neurophysiology*, **40**, 410-427.

Edwards, D.P., Purpura, K.P., & Kaplan, E. (1995). Contrast sensitivity and spatial frequency response of primate cortical neurons in and around the cytochrome oxidase blobs. *Vision Research*, **35**, 1501-1523.

Enroth-Cugell, C., & Shapley, R.M. (1973a). Adaptation and dynamics of cat retinal ganglion cells. *Journal of Physiology*, **233**, 271–309.

Enroth-Cugell, C., & Shapley, R.M. (1973b). Flux, not retinal illumination, is what cat retinal ganglion cells really care about. *Journal of Physiology*, **233**, 311-326.

Erisir, A., Van Horn, S.C., Bickford, M.E., & Sherman, S.M. (1997). Immunocytochemistry and distribution of parabrachial terminals in the lateral geniculate nucleus of the cat: a comparison with corticogeniculate terminal. *Journal of Comparative Neurology*, **377**, 535-549.

Erwin, E., Baker, F.H., Busen, W.F., & Malpeli, J.G. (1999). Relationship between laminar topology and retinotopy in the rhesus lateral geniculate nucleus: results from a functional atlas. *Journal of Comparative Neurology*, **407**, 92-102.

Eysel, U.T., Pape, H.C. & Van Schayck, R. (1986). Excitatory and differential disinhibitory actions of acetylcholine in the lateral geniculate nucleus of the cat. *Journal of Physiology*, **370**, 233-254.

Eysel, U.T., & Schweigart, G. (1999). Increased receptive field size in the surround of chronic lesions in the adult cat visual cortex. *Cerebral Cortex*, **9**, 101-109.

Fahrenfort, I., Habets, R.L., Spekreijse, H., & Kamermans, M. (1999). Intrinsic cone adaptation modulates feedback efficiency from horizontal cells to cones. *Journal of General Physiology*, **114**, 511-24.

Fain, G.L. (2001), Dark adaptation. *Progress in Brain Research*, **131**, 383-394.

Feigenspan, A., Wassle, H., & Bormann, J. (1993). Pharmacology of GABA receptor Cl^- channels in rat retinal bipolar cells. *Nature*, **361**, 159-162.

Felisberti, F., & Derrington, A.M. (2001). Long-range interactions in the lateral geniculate nucleus of the New-World monkey, Callithrix jacchus. *Visulal Neuroscience*, **18**, 209-218.

Felleman, D.J., & Van Essen, D.C. (1991). Distributed hierarchical processing in the primate cerebral cortex. *Cerebral Cortex*, **1**, 1-47.

Ferster, D., Chung, S., & Wheat, H. (1996). Orientation selectivity of thalamic input to simple cells of cat visual cortex. *Nature*, **380**, 249-252.

Field, D.J., Hayes, A., & Hess, R.F. (1993). Contour integration by the human visual system: evidence for a local "association field". *Vision Research*, **33**, 173-193.

Foster, K.H., Gaska, J.P., Nagler, M., & Pollen, D.A. (1985). Spatial and temporal frequency selectivity of neurones in visual cortical areas V1 and V2 of the macaque monkey. *Journal of Physiology*, **365**, 331-363.

Friedman, H.S., Zhou, H., & Von Der Heydt, R. (2003). The coding of uniform colour figures in monkey visual cortex. *Journal of Physiology*.

Fry, G.A. (1948). Mechanisms subserving simultaneous brightness contrast. *American Journal of Optometry and Archieves of the American Academy of Optometry*, **25**, 162-178.

Fry, G.A., & Alpern, M. (1953). The effect of a peripheral glare source upon the apparent brightness of an object. *Journal of the Optical Society of America*, **43**, 189-195.

Ghose, G.M., & Ts'o, D.Y. (1997). Form processing modules in primate area V4. *Journal Neurophysiology*, 77, 2191-2196.

Gilbert, C.D. (1977). Laminar differences in receptive field properties of cells in cat primary visual cortex. *Journal of Physiology (Lond)*, **268**, 391–421.

Gilbert, C.D., & Wiesel, T.N. (1979). Morphology and intracortical projections of functionally characterized neurones in the cat visual cortex. *Nature*, **280**, 120–125.

Gilchrist, A.L. (1977). Perceived lightness depends on perceived spatial arrangement. *Science*, **195**, 185-187.

Gilchrist, A.L. (1980). When does perceived lightness depend on perceived spatial arrangement? *Perception & Psychophysics*, **28**, 527-538.

Gilchrist, A.L., & Bonato, F. (1995). Anchoring of lightness values in center-surround displays. *Journal of Experimental Psychology - Human Perception and Performance*, **6**, 1427-1440.

Gilchrist, A.L., & Cataliotti, J. (1994). Anchoring of surface lightness with multiple illumination levels. *Investigative Ophthalmology and Visual Science*, **35**, S2165.

Gilchrist, A.L., Delman, S., & Jacobsen, A. (1983). The classification and integration of edges as critical to the perception of reflectance and illumination. *Perception & Psychophysics*, **33**, 425-436.

Gilchrist, A.L., Kossyfidis, C., Bonato, F., Agostini, T., Cataliotti, J., Li, X., Spehar, B., Annan, V., & Economou, E. (1999). An anchoring theory of lightness perception. *Psychological Review*, **106**, 795-834.

Gove, A., Grossberg, S., & Mingolla, E. (1995). Brightness perception, illusory contours, and corticogeniculate feedback. *Visual Neuroscience*, **12**, 1027-1052.

Grossberg, S. (1980). How does a brain build a cognitive code? *Psychological Review*, **87**, 1-51.

Grossberg, S. (1983). The quantized geometry of visual space: The coherent computation of depth, form and lightness. *Behavioral & Brain Sciences*, **6**, 625-692.

Grossberg, S. (1994). 3-D vision and figure-ground separation by visual cortex. *Perception & Psychophysics*, **55**, 48-120.

Grossberg, S. (2000). The complementary brain: unifying brain dynamics and modularity. *Trends in Cognitive Sciences*, **4**, 233-246.

Grossberg S. (2003). Filling-in the forms: Surface and boundary interactions in visual cortex. In *Filling-in: From Perceptual Completion to Skill Learning* (eds., Pessoa, L & De Weerd P.). New York: Oxford University Press.

Grossberg S., & Howe, P.D.L. (2003). A laminar cortical model of stereopsis and three-dimensional surface perception. *Vision Research*, **43**, 801-829.

Grossberg, S., Hwang, S., & Mingolla, E. (2002). Thalamocortical dynamics of the McCollough effect: boundary-surface alignment through perceptual learning. *Vision Research*, **42**, 1259-1286.

Grossberg, S., & Kelly, F. (1999). Neural dynamics of binocular brightness perception. *Vision Research*, **39**, 3796-3816.

Grossberg, S. & McLoughlin, N. (1997). Cortical dynamics of 3-D surface perception: Binocular and half-occluded scenic images. *Neural Networks*, **10**, 1583-1605.

Grossberg, S., & Mingolla, E. (1985a). Neural dynamics of perceptual grouping: textures, boundaries, and emergent segmentations. *Perception & Psychophysics*. **38**, 141-71.

Grossberg, S., & Mingolla, E. (1985b). Neural dynamics of form perception: boundary completion, illusory figures, and neon color spreading. *Psychological Review*, **92**, 173-211.

Grossberg, S., Mingolla, E., & Williamson, J. (1995). Synthetic aperture radar processing by a multiple scale neural system for boundary and surface representation. *Neural Networks*, **7/8**, 1005-1028.

Grossberg, S., & Raizada, R.D. (2000). Contrast-sensitive perceptual grouping and object-based attention in the laminar circuits of primary visual cortex. *Vision Research*, **40**, 1413-1432.

Grossberg, S., & Todorović, D. (1988). Neural dynamics of 1-D and 2-D brightness perception: a unified model of classical and recent phenomena. *Perception & Psychophysics*, **43**, 241–277.

Hahnloser, R.H., Douglas, R.J., & Hepp, K. (2002). Attentional recruitment of inter-areal recurrent networks for selective gain control. *Neural Computation*, **14**, 1669-1689.

Helmholtz, H. von, (1866). *Helmholtz's treatise on physiological optics*, New York: Optical Society of America.

Helson, H. (1943). Some factors and implications of color constancy. *Journal of the Optical Society of America*, **33**, 179-184.

Hering, E. (1920). Outline of a theory of the light sense, *trans. Hurvich, L. & Jameson, D. (1964)* (Harvard Univ. Press, Cambridge, MA).

Hong S, & Grossberg S (2003). Cortical Dynamics of Surface Lightness Anchoring, Filling-In, and Perception. *Vision Sciences Society, Third Annual Meeting, Sarasota, Florida*. pp. 120.

Hong S, & Grossberg S (2003). A neuromorphic model for achromatic and chromatic surface perception of natural images. Submitted for publication.

Horn, B.K.P. (1977). Understanding image intensities. *Artificial Intelligence*, **21**, 201-231.

Huang, X., MacEvoy, S.P., & Paradiso, M.A. (2002). Perception of brightness and brightness illusions in the macaque monkey. *Journal of Neuroscience*, **22**, 9618-9625.

Hubel, D.H. & Wiesel, T.N. (1961). Integrative action in the cat's lateral geniculate body. *Journal of Physiology*, **155**, 385-398.

Hubel, D.H. & Wiesel, T.N. (1962). Receptive fields, binocular interaction and functional architecture in the cat's visual cortex. *Journal of Physiology (London)*, **160**, 106-154.

Hung, C.P., Ramsden, B.M., Chen, L.M., & Roe, A.W., (2001). Building surfaces from borders in Areas 17 and 18 of the cat. *Vision Research*, **41**, 1389-1407.

Hurlbert, A.C. (1989). The computation of color, doctoral thesis. MIT.

Hurley, J.B. (2002). Shedding light on adaptation. *Journal of General Physiology*, **119**, 125-128.

Hupé, J.M., James, A.C., Payne, B.R., Lomber, S.G., Girard, P., & Bullier, J. (1998). Cortical feedback improves discrimination between figure and background by V1, V2 and V3 neurons. *Nature*, **394**, 784-787.

Hupé, J.M., James, A.C., Girard, P., & Bullier, J. (2001). Response modulations by static texture surround in area V1 of the macaque monkey do not depend on feedback connections from V2. *Journal of Neurophysiology*, **85**, 146-63.

Issa N.P., Trepel, C., & Stryker, M.P., (2000). Spatial frequency maps in cat visual cortex. *Journal of Neuroscience*, **20**, 8504-8514.

Jameson, D., & Hurvich, L.M. (1989). Essay concerning color constancy. *Annual Review of Psychology*, **40**, 1-22.

Jobson, D.J., Rahman, Z., & Woodell, G.A. (1997a). Properties and Performance of a Center/Surround Retinex. *IEEE Transactions on Image Processing*, March.

Jobson, D.J., Rahman, Z., & Woodell, G.A. (1997b). A Multi-Scale Retinex For Bridging the Gap Between Color Images and the Human Observation of Scenes. *IEEE Transactions on Image Processing: Special Issue on Color Processing*, July.

Johnson, R.R., & Burkhalter, A. (1997). A polysynaptic feedback circuit in rat visual cortex. *Journal of Neuroscience*, **17**, 7129-7140.

Jones, E.G., (1994). GABA neurons and their role in activity-dependent plasticity of adult primate visual cortex. In *Cerebral Cortex,* ed. A Peters, KS Rockland, **10**, 61-140. New York: Plenum.

Jones, H.E., Andolina, I.M., Oakely, N.M., Murphy, P.C., & Sillito, A.M. (2000). Spatial summation in lateral geniculate nucleus and visual cortex. *Experimental Brain Research*, **135**, 279-284.

Kaas, J.H., & Collins, C.E. (2001). The organization of sensory cortex. *Current Opinion in Neurobiology*, **11**, 498-504.

Kahrilas, P.J., Doty, R.W., & Bartlett, J.R. (1980). Failure to find luxotonic responses for single units in visual cortex of the rabbit. *Experimental Brain Research*, **39**, 11-16.

Kamermans, M., Haak, J., Habraken, JB., & Spekreijse, H. (1996). The size of the horizontal cell receptive fields adapts to the stimulus in the light adapted goldfish retina. *Vision Research*, **36**, 4105-4119.

Kamitani, Y., & Shimojo, S. (inpress). Global yet early processing of visual surfaces. In *The Visual Neurosciencies* (eds. Chalupa, L.M. & Werner, J.S.), MIT Press.

Kayama, Y., Riso, R.R., Bartlett, J.R., & Doty, R.W. (1979). Luxotonic responses of units in macaque striate cortex. *Journal of Neurophysiology*, **42**, 1495-1517.

Kellman, P.J., & Shipley, T.F. (1991). A theory of visual interpolation in object perception. *Cognitive Psychology*, **23**, 141-221.

Kelly, F., & Grossberg, S., (2000). Neural dynamics of 3-D surface perception: figure-ground separation and lightness perception. *Perception & Psychophysics*, **62**, 1596-1618.

Kimmel, R., Elad, M., Shaked, D., Keshet, R. & Sobel, I. (2002). A Variational Framework to Retinex. *The International Journal on Computer Vision*, July.

Kinoshita, M., & Komatsu, H. (2001). Neural representation of the luminance and brightness of a uniform surface in the macaque primary visual cortex. *Journal of Neurophysiology*, **86**, 2559-2570.

Kobatake, E., & Tanaka, K. (1994). Neuronal selectivities to complex object feature, in the ventral visual pathway of the macaque cerebral cortex. *Journal of Neurophysiology*, **71**, 856-867.

Kobayashi, M., Imamura, K., Sugai, T., Onoda, N., Yamamoto, M., Komai, S., & Watanabe, Y. (2000). Selective suppression of horizontal propagation in rat visual cortex by norepinephrine. *European Journal of Neuroscience*, **12**, 264-272.

Koffka, K. (1935). *Principles of Gestalt Psychology*, New York: Harcourt, Brace and Co.

Koutalos, Y., & Yau, K.W. (1996). Regulation of sensitivity in vertebrate rod photoreceptors by calcium. *Trends in Neuroscience*, **19** , 73-81.

Komatsu, H., Kinoshita, M., & Murakami, I. (2000). Neural Responses in the Retinotopic Representation of the Blind Spot in the Macaque V1 to Stimuli for Perceptual Filling-In. *Journal of Neuroscience*, **20**, 9310-9319.

Komatsu, H., Murakami, I., & Kinoshita, M. (1996). Surface representation in the visual system. *Cognitive Brain Research*, **5**, 97-104.

Kuffler, S.W. (1953). Discharge patterns and functional organization of mammalian retina. *Journal of Neurophysiology*, **16**, 37-68.

Lamme, V.A., (2001). Blindsight: the role of feedforward and feedback corticocortical connections. *Acta Psychologica (Amsterdam)*, **107**, 209-228.

Lamme, V.A., Zipser, K., & Spekreijse, H. (1998). Figure-ground activity in primary visual cortex is suppressed by anesthesia. *Proc Natl Acad Sci* U S A, **95**, 3263-3268.

Land, E.H., & McCann, J.J. (1971). Lightness and Retinex theory, *Journal of the Optical Society of America*, **61**, 1-11.

Lee, A.B., Blais, B., Shouval, H.Z., & Cooper, L.N., (2000). Statistics of lateral geniculate nucleus (LGN) activity determine the segregation of ON/OFF subfields for simple cells in visual cortex. *Proc Natl Acad Sci U S A*, **97**, 12875-12879.

Lee, B.B., Dacey, D.M., Smith, V.C., & Pokorny, J. (1999). Horizontal cells reveal cone type-specific adaptation in primate retina. *Proc Natl Acad Sci U S A*, **96**, 14611-14616.

Legg, C.R., & Cowey, A. (1977a). Effects of subcortical lesions on visual intensity discriminations in rats. *Physiology & Behavior,* **19**, 635-646.

Legg, C.R., & Cowey, A. (1977b). The role of the ventral lateral geniculate nucleus and posterior thalamus in intensity discrimination in rats. *Brain Research*, **123**, 261-273.

Libowitz, H. Mote, F.A. & Thurlow, W.R. (1953). Simultaneous contrast as a function of separation between test and inducing fields. *Journal of Experimental Psychology*, **46**, 453-456.

Livingstone, M. S. & Hubel, D. H. (1981). Effects of sleep and arousal on the processing of visual information in the cat. *Nature*, **291**, 554-561

Lu, C., Zhang, D.Q., & McMahon, D.G. (1999). Electrical coupling of retinal horizontal cells mediated by distinct voltage-independent junctions. *Visual Neuroscience*, **16**, 811-818

MacEvoy, S.P., Kim, W., & Paradiso, M.A. (1998). Integration of surface information in primary visual cortex. *Nature Neuroscience*, **1**, 616-620.

MacEvoy, S.P., & Paradiso, M.A. (2001). Lightness constancy in primary visual cortex. *Proc Natl Acad Sci USA*, **98**, 8827-8831.

Marrocco, R.T. (1972). Maintained activity of monkey optic tract fibers and lateral geniculate nucleus cells. *Vision Research*, **12**, 1175-1181.

Martin, G.R. (1983). Schematic eye models in vertebrates. *Progress in Sensory Physiology*, **4**, 44–81.

Martinez, L.M., & Alonso, J.M. (2001). Construction of complex receptive fields in cat primary visual cortex. *Neuron*, **32**, 515-525.

Masland, R.H. (2001). The fundamental plan of the retina. *Nature Neuroscience*, **4**, 877-886.

McMahon, D.G. (1994). Modulation of electrical synaptic transmission in zebrafish retinal horizontal cells. *Journal of Neuroscience*. **14**, 1722-1734

McMahon, D.G., Zhang, D.Q., Ponomareva, L., & Wagner, T. (2001). Synaptic mechanisms of network adaptation in horizontal cells. *Progress in Brain Research*, **131**, 419-436

Mechler, F., & Ringach, D.L. (2002). On the classification of simple and complex cells. *Vision Research*, **42**, 1017-1033.

Meister, M., & Berry, M.J. 2nd (1999). The neural code of the retina. *Neuron*, **22**, 435-450.

Mills, S.L., & Massey, S.C. (1995). Differential properties of two gap junctional pathways made by AII amacrine cells. *Nature*, **377**, 734-737.

Mingolla, E., Ross, W., & Grossberg, S., (1999). A neural network for enhancing boundaries and surfaces in synthetic aperture radar images. *Neural Networks*, **12**, 499-511.

Moore, R.Y., Weis, R., & Moga, M.M. (2000). Efferent projections of the intergeniculate leaflet and the ventral lateral geniculate nucleus in the rat. *Journal of Comparative Neurology*, **420**, 398-418.

Naka, K.I., & Rushton, W.A. (1967). The generation and spread of S-potentials in fish (Cyprinidae). *Journal of Physiology*, **192**, 437-461.

Nakamura, H., Gattass, R., Desimone, R., & Ungerleider, L.G. (1993). The modular organization of projections from areas V1 and V2 to areas V4 and TEO in macaques. *Journal of Neuroscience*, **13**, 3681-3691.

Nakatani, K., Tamura, T., & Yau, K.W. (1991). Light adaptation in retinal rods of the rabbit and two other nonprimate mammals. *Journal of General Physiology*, **97**, 413–435.

Nakayama, K., & Shimojo, S. (1992). Experiencing and perceiving visual surfaces. *Science*, **257**, 1357-1363.

Nawy, S. (2000). Regulation of the on bipolar cell mGluR6 pathway by Ca^{2+}. *Journal of Neuroscience*, **20**, 4471-4479

Neumann, H., Pessoa, L., & Hansen, T. (2001). Visual filling-in for computing perceptual surface properties. *Biological Cybernetics*, **85**, 355-369.

Neumann, H., & Sepp, W. (1999). Recurrent V1–V2 interaction in early visual boundary processing. *Biological Cybernetics,* **81**, 425–444.

Newson, L.J. (1958). Some principles governing changes in the apparent lightness of test surfaces isolated from their normal backgrounds. *Quarterly Journal of Experimental Psychology*, **10**, 82-95.

Papaioannou, J., & White, A. (1972). Maintained activity of lateral geniculate ucleus neurons as a function of background luminance. *Experimental Neurology*, **34**, 558-566.

Paradiso, M.A., & Nakayama, K. (1991). Brightness perception and filling-in. *Vision Research*, **31**, 1221-1236.

Pessoa, L., Mingolla, E., & Arend, L.E. (1996). The perception of lightness in 3-D curved objects. *Perception & Psychophysics*, **58**, 1293-1305.

Pessoa, L., Mingolla, E., & Neumann, H. (1995). A contrast- and luminance-driven multiscale network model of brightness perception. *Vision Research*, **35**, 2201-2223.

Pessoa, L., & Neumann, H. (1998). Why does the brain fill-in? *Trends in Cognitive Sciences*, **11**, 422-424.

Peterhans, E., von der Heydt, R. (1989). Mechanisms of contour perception in monkey visual cortex. II. Contours bridging gaps. *Journal of Neuroscience*, **9**, 1749-1763.

Pinna, B., Brelstaff, G., & Spillmann, L. (2001). Surface color from boundaries: a new 'watercolor' illusion. *Vision Research*, **41**, 2669-2676.

Pinna, B., Werner, J.S., & Spillmann, L. (2003). The watercolor effect: a new principle of grouping and figure-ground organization. *Vision Research*, **43**, 43-53.

Posner, M.I., Snyder, C.R.R. & Davidson, B.J. (1980). Attention and the detection of signals. *Journal of Experimental Psychology*, **109**, 160-174

Przybyszewski, A.W., Gaska, J.P., Foote, W., & Pollen, D.A. (2000). Striate cortex increases contrast gain of macaque LGN neurons. *Visulal Neuroscience*, **17**, 485-494.

Raizada, R.D.S. & Grossberg, S. (2001). Context-sensitive binding by the laminar circuits of V1 and V2: A unified model of perceptual grouping, attention, and orientation contrast. *Visual Cognition*, **8**, 431-466.

Raizada, R.D.S. & Grossberg, S. (2003). Towards a theory of the laminar architecture of cerebral cortex: computational clues from the visual system. *Cerebral Cortex*, **13**, 100-113.

Reid, R.C., & Alonso, J.M. (1995). Specificity of monosynaptic connections from thalamus to visual cortex. *Nature*, **378**, 281-284.

Reynolds, J.H., Chelazzi, L., & Desimone, R. (1999). Competitive mechanisms subserve attention in macaque areas V2 and V4. *Journal of Neuroscience*, **19**, 1736-1753.

Ribelayga, C., Wang, Y., & Mangel, S.C. (2002). Dopamine mediates circadian clock regulation of rod and cone input to fish retinal horizontal cells. *Journal of Physiology*, **544**, 801-816.

Ringach, D.L. (2002). Spatial structure and symmetry of simple-cell receptive fields in macaque primary visual cortex. *Journal of Neurophysiology*, **88**, 455-463.

Rockland, K.S., & Lund, J.S. (1982). Widespread periodic intrinsic connections in the tree shrew visual cortex. *Science*, **215**, 1532–1534.

Rodieck, R.W. (1965). Quantitative analysis of cat retinal ganglion cell response to visual stimuli. *Vision Research*, **5**, 583–601.

Rodieck, R.W., & Stone, J. (1965). Response of cat retinal ganglion cells to moving visual patterns. *Journal of Neurophysiology*, **28**, 819–832.

Roe, A.W., & Ts'o, D.Y. (1995). Visual topography in primate V2: multiple representation across functional stripes. *Journal of Neuroscience*, **15**, 3689-3715.

Roe, A.W. & Ts'o, D.Y., (1999). Specificity of color connectivity between primate V1 and V2. *Journal of Neurophysiology*, **82**, 2719–2730.

Roska, B., Nemeth, E., Orzo, L. & Werblin, F.S. (2000). Three levels of lateral inhibition: a space-time study of the retina of the tiger salamander. *Journal of Neuroscience*, **20**, 1941-1951.

Roska, B., & Werblin, F.S. (2001). Vertical interactions across ten parallel, stacked representations in the mammalian retina. *Nature*, **410**, 583-587.

Rossi, A.F., & Paradiso, M.A. (1999). Neural correlates of perceived brightness in the retina, lateral geniculate nucleus, and striate cortex. *Journal of Neuroscience*, **19**, 6145-6156

Rossi, A.F., Rittenhouse, C.D., & Paradiso, M.A. (1996). The representation of brightness in primary visual cortex. *Science*, **273**, 1104-1107.

Rozas, C., Frank, H., Heynen, A.J., Morales, B., Bear, M.F., & Kirkwood, A. (2001). Developmental inhibitory gate controls the relay of activity to the superficial layers of the visual cortex. *Journal of Neuroscience*, **21**, 6791-6801.

Ruksenas, O., Fjeld, I.T. & Heggellund, P. (2000). Spatial summation and center-surround antagonism in the receptive field of single units in the dorsal lateral geniculate nucleus of cat: Comparison with retinal input. *Visual Neuroscience*, **17**, 855 –870.

Sakai, K., & Tanaka, S. (2000). Spatial pooling in the second-order spatial structure of cortical complex cells. *Vision Research*, **40**, 855-871.

Sasaki, Y., Watanabe, T., Dale, A.M., & Tootell, R.B. (2001). V1 involvement for color filling-in revealed by human fMRI. *Society for Neuroscience Abstracts*:12.11.

Schiller, P.H. (1992). The ON and OFF channels of the visual system. *Trends in Neuroscience*, **15**, 86-92.

Schiller, P.H., Finlay, B.L., & Volman, S.F. (1976). Quantitative studies of single-cell properties in monkey striate cortex. V. Multivariate statistical analyses and models. *Journal of Neurophysiology*, **39**, 1362-1374.

Schiller, P.H., Sandell, J.H., & Maunsell, J.H. (1986). Functions of the ON and OFF channels of the visual system. *Nature*, **322**, 824-825.

Schirillo, J., Reeves, A., & Arend, L. (1990). Perceived lightness, but not brightness, of achromatic surfaces depends on perceived depth information. *Perception & Psychophysics*, **48**, 82-90.

Schwartz E. (1980). Computational anatomy and functional architecture of striate cortex: a spatial mapping approach to perceptual coding. *Vision Research*, ***20***, 645–699.

Shapley, R., & Enroth-Cugell, C. (1984). Visual adaptation and retinal gain controls. *Progress in Retinal Research*, **3**, 263–346.

Sherman, S.M. (1996). Dual response modes in lateral geniculate neurons: mechanisms and functions. *Visual Neuroscience*, **13**, 205–213.

Sherman, S.M. (2001). Tonic and burst firing: dual modes of thalamocortical relay. *Trends in Neuroscience*, **24**, 122-126.

Shevelev, I.A. (1998). Second-order feature extraction in the cat visual cortex: selective and invariant sensitivity of neurons to the shape and orientation of crosses and corners. *Biosystems*, **48**, 195-204.

Shevelev, I.A. (2000). Sensitivity of striate neurons to Y-like figures: experiment and simulation. *Biosystems*, **58**, 211-217.

Shevelev, I.A., Lazareva, N.A., Sharaev, G.A., Novikova, R.V., & Tikhomirov, A.S. (1998). Selective and invariant sensitivity to crosses and corners in cat striate neurons. *Neuroscience*, **84**, 713-721.

Sillito, A.M., Jones, H.E., & Gerstein, G.L. (1994). West DC, Feature-linked synchronization of thalamic relay cell firing induced by feedback from the visual cortex. *Nature*, **369**, 479-482.

Sillito, A.M., Kemp, J.A. & Beradi, N. (1983). The cholinergic influence on the function of the cat dorsal lateral geniculate nucleus (dLGN). *Brain Research*, **280**, 299 –307.

Smirnakis, S.M., Berry, M.J., Warland, D.K., Bialek, W., & Meister, M. (1997). Adaptation of retinal processing to image contrast and spatial scale. *Nature*, **386**, 69-73.

Solomon, S.G., White, A.J., Martin, P.R. (2002). Extraclassical receptive field properties of parvocellular, magnocellular, and koniocellular cells in the primate lateral geniculate nucleus. *Journal of Neuroscience*, **22**, 338-349.

Somers, D.C., Dale, A.M., Seiffert, A.E., & Tootell, R.B. (1999). Functional MRI reveals spatially specific attentional modulation in human primary visual cortex. *Proc Natl Acad Sci USA*, **96**, 1663-1668.

Somers, D.C., Todorov, E.V., Siapas, A.G., Toth, L.J., Kim, D.S., & Sur, M., (1998). A local circuit approach to understanding integration of long-range inputs in primary visual cortex. *Cerebral Cortex*, **8**, 204-217.

Spillmann, L. (1994). The Hermann Grid Illusion: a Tool for Studying Human Perceptive Field Organization. *Perception*, **23**, 691-708.

Spray, D.C., Harris A.L., & Bennett M.V. (1979). Voltage dependence of junctional conductance in early amphibian embryos. *Science*, **204**, 432-434.

Stanley, G.B., Li, F.F., & Dan, Y. (1999). Reconstruction of natural scenes from ensemble responses in the lateral geniculate nucleus. *Journal of Neuroscience*, **19**, 8036-8042.

Sterling, P. in *The Synaptic Organization of the Brain* Vol. 4 (ed. Shepherd, G. M.), 205-253 (Oxford Univ. Press, New York, 1998).

Stettler, D.D., Das, A., Bennett, J., & Gilbert, C.D. (2002). Lateral connectivity and contextual interactions in macaque primary visual cortex. *Neuron*, **36**, 739-750.

Suder, K., Wörgötter, F., & Wennekers, T. (2001). Neural field model of receptive field restructuring in primary visual cortex. *Neural Computation*, **13**, 139-159.

Tadmor, Y., & Tolhurst, D.J. (2000). Calculating the contrasts that retinal ganglion cells and LGN neurons encounter in natural scenes. *Vision Research*, **40**, 3145-3157.

Thibos, L.N., & Werblin, F.S. (1978). The response properties of the steady antagonistic surround in the mudpuppy retina. *Journal of Physiology*, **278**, 79-99.

Todorović, D. (1997). Lightness and junctions. *Perception*, **26**, 379-394.

Tomita, T. (1965). Electrophysiological study of the mechanisms subserving color coding in the fish retina. *Cold Spring Harbor Symposium on Quantitative Biology*, **30**, 559-66.

Triesman, A.M. & Sato, S. (1990). Conjunction search revisited. *Journal Of Experimental Psychology-Human Perception And Performance*, **16**, 459-478

Troyer, T.W., Krukowski, A.E., Priebe, N.J., & Miller, K.D. (1998). Contrast-invariant orientation tuning in cat visual cortex: thalamocortical input tuning and correlation-based intracortical connectivity. *Journal of Neuroscience*, **18**, 5908-5927.

Ts'o, D.Y., Roe, A.W., & Gilbert, C.D. (2001). A hierarchy of the functional organization for color, form and disparity in primate visual area V2. *Vision Research*, **41**, 1333-1349.

Usrey, W.M., Sceniak, M.P., & Chapman, B. (2003). Receptive fields and response properties of neurons in layer 4 of ferret visual cortex. *Journal of Neurophysiology*, **89**, 1003-1015.

Verweij, J., Kamermans, M., & Spekreijse, H. (1996). Horizontal cells feed back to cones by shifting the cone calcium-current activation range. *Vision Research*, **36**, 3943-3953.

von der Heydt, R., Peterhans, E., & Baumgartner, G. (1984). Illusory contours and cortical neuron responses. *Science*, **224**, 1260-1262.

Wallach, H. (1948). Brightness constancy and the nature of achromatic colors. *Journal of Experimental Psychology*, **38**, 310-324.

Wallach, H. (1976). *On perception*, New York: Quadrangle/The New Your Times Book Co.

Welchman, A.E., & Harris, J.M. (2001). Filling-in the details on perceptual fading. *Vision Research*, **41**, 2107-2117.

Werblin, F.S. (1971). Adaptation in a vertebrate retina: intracellular recording in Necturus. *Journal of Neurophysiology*, **34**, 228-241.

Werblin, F.S. (1974). Control of retinal sensitivity. II. Lateral interactions at the outer plexi form layer. *Journal of General Physiology*, **63**, 62-87.

Werblin, F.S., & Dowling, J.E. (1969). Organization of the retina of the mudpuppy. *Necturus maculosus*. II. Intracellular recording. *Journal of Neurophysiology*, **32**, 339-355.

Werblin, F.S., Roska, B., & Balya, D. (2001). Parallel processing in the mammalian retina: lateral and vertical interactions across stacked representations. *Progress in Brain Research*, **131**, 229-238.

Witkovsky, P. & Dearry A. (1991). Functional roles of dopamine in the vertebrate retina. *Progress in Retinal Research*, **11**, 247–292.

Wörgötter, F., Suder, K., Zhao, Y., Kerscher, N., Eysel, U.T., & Funke, K. (1998). State-dependent receptive-field restructuring in the visual cortex. *Nature*, **396**, 165-8.

Xin, D., & Bloomfield, S.A. (1999). Dark- and light-induced changes in coupling between horizontal cells in mammalian retina. *Journal of Comparative Neurology*, **405**, 75-87.

Xin, D., & Bloomfield, S.A. (2000). Effects of nitric oxide on horizontal cells in the rabbit retina. *Visual Neuroscience*. **17**, 799-811.

Yarbus, A.L. (1967). *Eye movements and vision*. Plenum Press.

Yabuta, N.H., & Callaway, E.M. (1998). Cytochrome-oxidase blobs and intrinsic horizontal connections of layer 2/3 pyramidal neurons in primate V1. *Visual Neuroscience*. **15**, 1007-1027.

Zhou, H., Friedman, H.S., & von der Heydt, R. (2000). Coding of border ownership in monkey visual cortex. *Journal of Neuroscience*, **20**, 6594-6611.

Zipser, K., Lamme, V.A., & Schiller, P.H. (1996). Contextual modulation in primary visual cortex. *Journal of Neuroscience*, **16**, 7376-7389.